nature chemical biology

Article

https://doi.org/10.1038/s41589-024-01689-z

Phospholipid biosynthesis modulates nucleotide metabolism and reductive capacity

Received: 21 August 2023

Accepted: 2 July 2024

Yibing Zhu[1,6], Xiaomeng Tong[1,6], Jingyuan Xue[1,6], Hong Qiu[1], Dan Zhang [2], Dao-Qiong Zheng[3,4], Zong-Cai Tu[5] & Cunqi Ye [1,2,4,5] ✉

Phospholipid and nucleotide syntheses are fundamental metabolic processes in eukaryotic organisms, with their dysregulation implicated in various disease states. Despite their importance, the interplay between these pathways remains poorly understood. Using genetic and metabolic analyses in *Saccharomyces cerevisiae*, we elucidate how cytidine triphosphate usage in the Kennedy pathway for phospholipid synthesis influences nucleotide metabolism and redox balance. We find that deficiencies in the Kennedy pathway limit nucleotide salvage, prompting compensatory activation of de novo nucleotide synthesis and the pentose phosphate pathway. This metabolic shift enhances the production of antioxidants such as NADPH and glutathione. Moreover, we observe that the Kennedy pathway for phospholipid synthesis is inhibited during replicative aging, indicating its role in antioxidative defense as an adaptive mechanism in aged cells. Our findings highlight the critical role of phospholipid synthesis pathway choice in the integrative regulation of nucleotide metabolism, redox balance and membrane properties for cellular defense.

Phospholipids are the major components of cell membranes and are synthesized for membrane expansion and remodeling to ensure cell growth and adaptive transition[1–3]. While an obvious role of the regulation of phospholipid synthesis is to generate cell membranes of unique lipid compositions, how this regulatory control necessitates metabolic coordination remains an open question and poorly understood.

Phospholipids are polar glycerolipids consisting of a hydrophilic phosphate group head and hydrophobic fatty acid tails joined by a glycerol backbone, primarily synthesized in the endoplasmic reticulum (ER)[2,4]. The pathways for producing phospholipids with different head group classes are mostly conserved among eukaryotic kingdoms and best studied in the budding yeast *Saccharomyces cerevisiae*[5–9]. The most abundant phospholipids in cell membranes, phosphatidylethanolamine (PE) and phosphatidylcholine (PC), are synthesized through the Kennedy pathway[9–12] or the cytidine diphosphate–diacylglycerol (CDP–DAG) pathway. In a sequential reaction, PE is generated by the decarboxylation of the phospholipid phosphatidylserine (PS)[13–15] and subsequently converted to PC through methylation[16,17]. DAG and phosphatidic acid (PA) act as lipid precursors in two biosynthetic processes, with cytidine triphosphate (CTP) partitioning synthesis to discrete activations of either soluble metabolites or a lipid precursor[11,18].

Curiously, different nucleoside triphosphates (NTPs) have evolved specific functions beyond RNA synthesis. ATP is mainly used to power endergonic reactions and to regulate cellular processes through protein phosphorylation. Guanosine triphosphate (GTP) and uridine triphosphate (UTP) are used for the regulation of signal transduction and sugar metabolism, respectively[19,20]. The significance of the involvement of CTP in driving phospholipid synthesis remains enigmatic. In this study, we

---

[1]Zhejiang Provincial Key Laboratory for Cancer Molecular Cell Biology, Life Sciences Institute, Zhejiang University, Hangzhou, China. [2]Department of Reproductive Endocrinology, Women's Hospital, Zhejiang University School of Medicine, Hangzhou, China. [3]Ocean College, Zhejiang University, Zhoushan, China. [4]Hainan Institute, Zhejiang University, Sanya, China. [5]National R&D Center for Freshwater Fish Processing, Jiangxi Normal University, Nanchang, China. [6]These authors contributed equally: Yibing Zhu, Xiaomeng Tong, Jingyuan Xue. ✉e-mail: yecunqi@zju.edu.cn

report that CTP usage in the Kennedy pathway establishes a metabolic modality, where phospholipid synthesis connects with nucleotide metabolism and antioxidant production. Our findings indicate that deficiencies in the Kennedy pathway disrupt nucleotide homeostasis, imposing constraints on nucleotide salvage and triggering compensatory activation of de novo nucleotide synthesis. This necessitates the co-activation of the pentose phosphate pathway (PPP), ultimately fostering the synthesis of antioxidants like NADPH and glutathione (GSH). Notably, a diminished flux in the Kennedy pathway is observed under replicative aging, showcasing a mechanism for antioxidative defense in aged cells. This study unveils the metabolic role of CTP in phospholipid synthesis, demonstrating its involvement in coupling the regulation of nucleotide salvage and ribose production to the generation of reducing equivalents.

Results

Blocking PA to DAG conversion disrupts nucleotide metabolism

To explore metabolic coordination with phospholipid pathways, we constructed deletion mutants *pah1Δ* and *dgk1Δ* in the prototrophic CEN.PK strain background. These mutants block the conversion between the two lipid precursors, PA and DAG, involved in the CDP–DAG pathway and the Kennedy pathway (Fig. 1a). Wild-type (WT) and mutant cells in the logarithmic (log) and stationary phases were collected for targeted metabolomics analysis (Fig. 1b). In agreement with previous findings[21,22], the *pah1Δ* mutant displayed a moderate growth defect in a synthetic defined (SD) minimal medium, while *dgk1Δ* cells displayed growth similar to WT cells (Fig. 1c). Principal component analysis (PCA) revealed distinct soluble metabolite compositions in the *pah1Δ* mutant in the log phase compared to WT and *dgk1Δ* cells (Fig. 1d). In the stationary phase, both *pah1Δ* and *dgk1Δ* mutants exhibited metabolic profiles different from WT cells (Fig. 1d), indicating unique metabolic impacts associated with DAG and PA-directed synthesis of phospholipids. Kyoto Encyclopedia of Genes and Genomes (KEGG) pathway analysis of differential metabolites in WT and the *pah1Δ* mutant highlighted enriched pathways such as arginine biosynthesis, purine metabolism and pyrimidine metabolism (Fig. 1e). In particular, *pah1Δ* substantially increased guanosine, inosine and cytidine monophosphate (CMP) levels while decreasing adenosine monophosphate (AMP) and inosine monophosphate (IMP) levels (Fig. 1f,g). This aberrant nucleotide metabolism in the *pah1Δ* mutant paralleled findings in *lipin1*-deficient mouse gastrocnemius muscles[23]. Furthermore, the *pah1Δ* mutant exhibited a 40–60-fold increase in CDP–choline and a 100–200-fold increase in CDP–ethanolamine (Fig. 1h). Under stationary stress conditions, these CDP metabolites levels further rose (Fig. 1h). CDP metabolites are necessary for PC and PE synthesis via the Kennedy pathway through an amino alcohol phosphotransferase (AAPT) reaction with DAG[9]. Consistent with reported studies in yeast[24,25] and other organisms[23,26] in the *pah1Δ* mutant, lipid profiling using liquid chromatography with tandem mass spectrometry (LC–MS/MS) confirmed substantial reductions in DAG and TAG levels (Fig. 1i) along with increases in PA and total phospholipid levels, causing a perturbed class composition (Extended Data Fig. 1a,b). Disruption of Pah1-mediated DAG production likely limited the availability of DAG for the Kennedy pathway[26,27], leading to the accumulation of CDP–choline and CDP–ethanolamine, a metabolic phenomenon known as pyrimidine cache[28].

Because the formation of the pyrimidine cache impedes pyrimidine salvage, *pah1Δ* cells were expected to become more reliant on the de novo pathway for pyrimidine nucleotide production (Fig. 1j). Indeed, when de novo synthesis of pyrimidine was blocked by *ura2Δ*, *ura1Δ* or *ura3Δ*, uracil supplementation improved the growth of the *pah1Δ* mutant (Fig. 1k). This effective restoration of growth in the lipodystrophy mutant was in line with its addictive usage of the de novo pathway for pyrimidine synthesis. Moreover, RNA sequencing revealed that most genes in pyrimidine biosynthesis were not transcriptionally affected by *dgk1Δ* or *pah1Δ* (Extended Data Fig. 1c–e and Supplementary Data 2 and 3), suggesting that the pyrimidine cache formation alone is sufficient to induce the de novo synthesis pathway. Overall, mRNA transcript profiles were more affected by *pah1Δ* than by *dgk1Δ* (Extended Data Fig. 1d,e). KEGG analysis showed that differentially expressed genes in the *pah1Δ* mutant were mostly associated with metabolic pathways (Extended Data Fig. 1f,g), indicating a coordinated transcriptional regulation of metabolic genes in this lipodystrophy mutant.

The Kennedy pathway maintains nucleotide homeostasis

To investigate the role of the Kennedy pathway in regulating nucleotide homeostasis, we constructed double knockout mutants *pct1Δect1Δ* and *cpt1Δept1Δ* to block two sequential steps in the pathway (Fig. 2a). Although the Kennedy pathway is responsible for PE and PC synthesis, it is dispensable for cell growth, even in minimal medium (Fig. 2b), because PE and PC can be alternatively synthesized through PS decarboxylation and PE methylation[5,6]. Next, we profiled intracellular levels of purine and pyrimidine metabolites. Compared to WT and the *cho2Δopi3Δ* mutant (which blocks the PE to PC conversion), disrupting the Kennedy pathway at either the CTP-based activation step (*pct1Δect1Δ*) or the final AAPT-mediated condensation step (*cpt1Δept1Δ*) resulted in increased levels of various nucleotide metabolites (Fig. 2c). Nucleotide quantification using MS revealed elevated levels of nucleoside monophosphate, diphosphate and triphosphate in both mutants, with CMP showing a 50-fold increase in *cpt1Δept1Δ* cells (Fig. 2d). In this mutant, CDP–choline increased approximately 400-fold and CDP–ethanolamine about 800-fold (Fig. 2e). Individual deletion of either enzyme did not cause such substantial increases (Extended Data Fig. 2a), consistent with previous studies indicating a partial functional overlap between Cpt1 and Ept1 (refs. 27–31).

To quantify the amount of cytosine nucleotide cached in the CDP bases, we performed reverse isotopic labeling (RIL). In the *cpt1Δept1Δ* mutant, CDP–choline and CDP–ethanolamine concentrations were approximately 0.25 mM and 0.85 mM, respectively (Fig. 2f), collectively constituting about 480% of cellular CTP and 120% of CMP. Compared to WT cells, the pyrimidine cache formation in *cpt1Δept1Δ* cells resulted in an overproduction of various cytosine nucleotides (Fig. 2g).

Despite the dysregulation of nucleotide metabolism, the *pct1Δect1Δ* and *cpt1Δept1Δ* mutants exhibited only a limited number of differentially expressed genes (Extended Data Fig. 2b,c and Supplementary Data 4 and 5), suggesting that Kennedy pathway deficiencies can induce metabolic reprogramming independent of substantial transcriptional regulation.

Kennedy pathway deficiency modestly alters membrane order

In contrast to the *pah1Δ* mutant, the blockage of the Kennedy pathway in the *cpt1Δept1Δ* mutant did not affect cell growth (Fig. 2b) and only modestly altered the composition levels of PE, PC and other phospholipid classes (Fig. 2h). Levels of PA and DAG remained unchanged, with marginal decreases in TAG levels and slight increases in total phospholipid levels (Extended Data Fig. 2d–g). However, the acyl composition of PC was notably altered in the *cpt1Δept1Δ* mutant (Extended Data Fig. 2h), showing a decrease in average acyl length and an increase in average unsaturation (Extended Data Fig. 2i,j). These changes likely promote membrane fluidity[32–34], which was consistent with the observed decrease in plasma membrane order in the Kennedy pathway-deficient mutant (Extended Data Fig. 2k).

Additionally, we observed that the turnover of Cho2, the first enzyme in the PE methylation pathway, was impeded 2 h after choline supplementation in *cpt1Δept1Δ* (Extended Data Fig. 2l). Disrupting the rate-limiting step of PC synthesis in the Kennedy pathway by *pct1Δ* also blocked Cho2 turnover (Extended Data Fig. 2l). This suggests that in the presence of exogenous choline, cells prefer the Kennedy pathway for PC synthesis, thereby reducing enzyme levels in the PE methylation pathway. We propose that the choice of the phospholipid synthesis pathway not only modulates membrane biophysical properties but also has a role in regulating nucleotide metabolism.

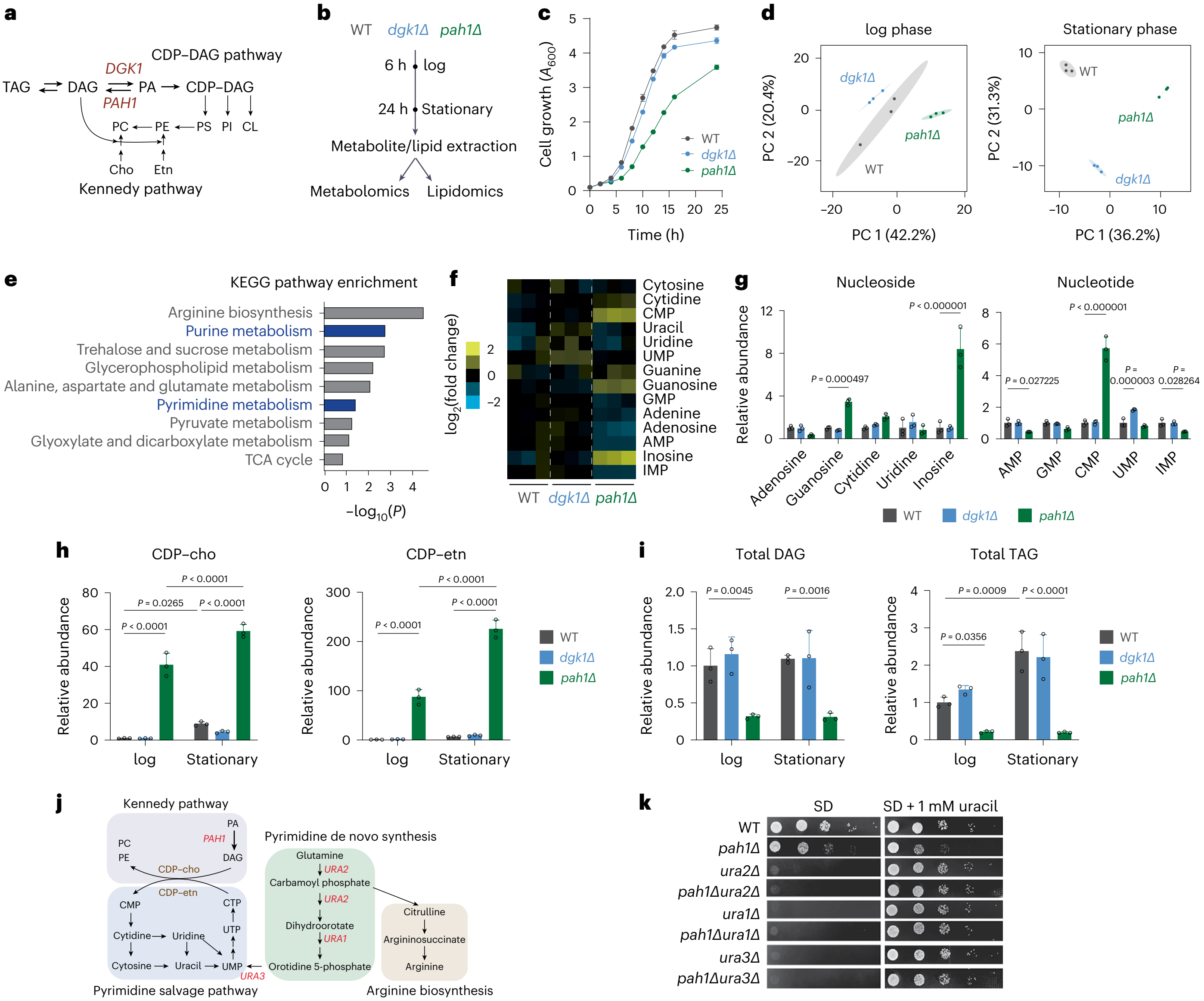

Fig. 1 | Disruption of the PA to DAG conversion impacts nucleotide metabolism. a, Schematic representation of phospholipid biosynthesis pathways in *S. cerevisiae*. **b**, Overview of metabolomics and lipidomics analyses conducted in WT, *dgk1Δ* and *pah1Δ* cells. **c**, Growth curves depicting the growth of WT, *dgk1Δ* and *pah1Δ* cells in minimal medium. Data are represented as mean ± s.d. ($n = 3$ biologically independent samples). **d**, PCA plots of metabolite profiles in WT, *dgk1Δ* and *pah1Δ* cells in the log phase (left) and the stationary phase (right). **e**, KEGG pathway analysis of differential metabolites in WT and *pah1Δ* cells. **f**, Heatmap displaying cellular abundances of nucleotide metabolites in WT, *dgk1Δ* and *pah1Δ* cells in the log phase. **g**, Relative abundance of nucleosides (left) and nucleotides (right) in WT, *dgk1Δ* and *pah1Δ* cells in the log phase. Data are presented as mean ± s.d. ($n = 3$ biologically independent samples). **h**, Relative abundance of CDP–choline and CDP–ethanolamine in WT, *dgk1Δ* and *pah1Δ* cells. Data are presented as mean ± s.d. ($n = 3$ biologically independent samples). **i**, Relative abundance of DAG and TAG in WT, *dgk1Δ* and *pah1Δ* cells in the log phase and stationary phase. Data are presented as mean ± s.d. ($n = 3$ biologically independent samples). **j**, Metabolic pathways highlighting intersections at the Kennedy pathway, pyrimidine salvage pathway, pyrimidine de novo synthesis and arginine biosynthesis. **k**, Growth of WT and indicated mutants on minimal medium with or without 1 mM uracil after incubation at 30 °C for 1 day. Source data are provided as a source data file. PI, phosphatidylinositol; CL, cardiolipin; cho, choline; etn, ethanolamine; TCA, tricarboxylic acid cycle.

Kennedy pathway deficiency boosts nucleotide synthesis

To further investigate how phospholipid synthesis influences nucleotide metabolism, we conducted tracing experiments using (U-^{13}C6) glucose to investigate the synthesis and turnover of purine and pyrimidine nucleotides (Extended Data Fig. 3a). In the *cpt1Δept1Δ* mutant, the levels of newly synthesized CMP, AMP and GMP were substantially increased compared to WT (Extended Data Fig. 3b). Notably, newly synthesized CMP showed a 25-fold increase in the mutant, contrasting with moderate increases in labeled AMP and GMP levels (Extended Data Fig. 3c). This accumulation of ^{13}C-labeled CMP was associated with reduced CMP turnover (Extended Data Fig. 3d), while AMP and GMP turnover remained similar (Extended Data Fig. 3d). The compromised turnover of CMP suggested a limitation in pyrimidine recycling, prompting upregulation of de novo synthesis as compensation.

Indeed, *cpt1Δept1Δ* cells exhibited increased production of ribose 5-phosphate (R5P), sedoheptulose 7-phosphate (S7P) and erythrose 4-phosphate (E4P; Extended Data Fig. 3e), confirming synergized PPP activity in supplying ribose for de novo nucleotide synthesis. Using 1,2-^{13}C2 glucose to assess glycolysis and PPP flux (Extended Data Fig. 3f), we observed substantial increases in $m + 2$ 6-phosphogluconate (6PG) and $m + 1$ R5P from the oxidative branch of PPP, along with $m + 2$ glucose 6-phosphate, $m + 2$ fructose 6-phosphate and $m + 2$ glyceraldehyde

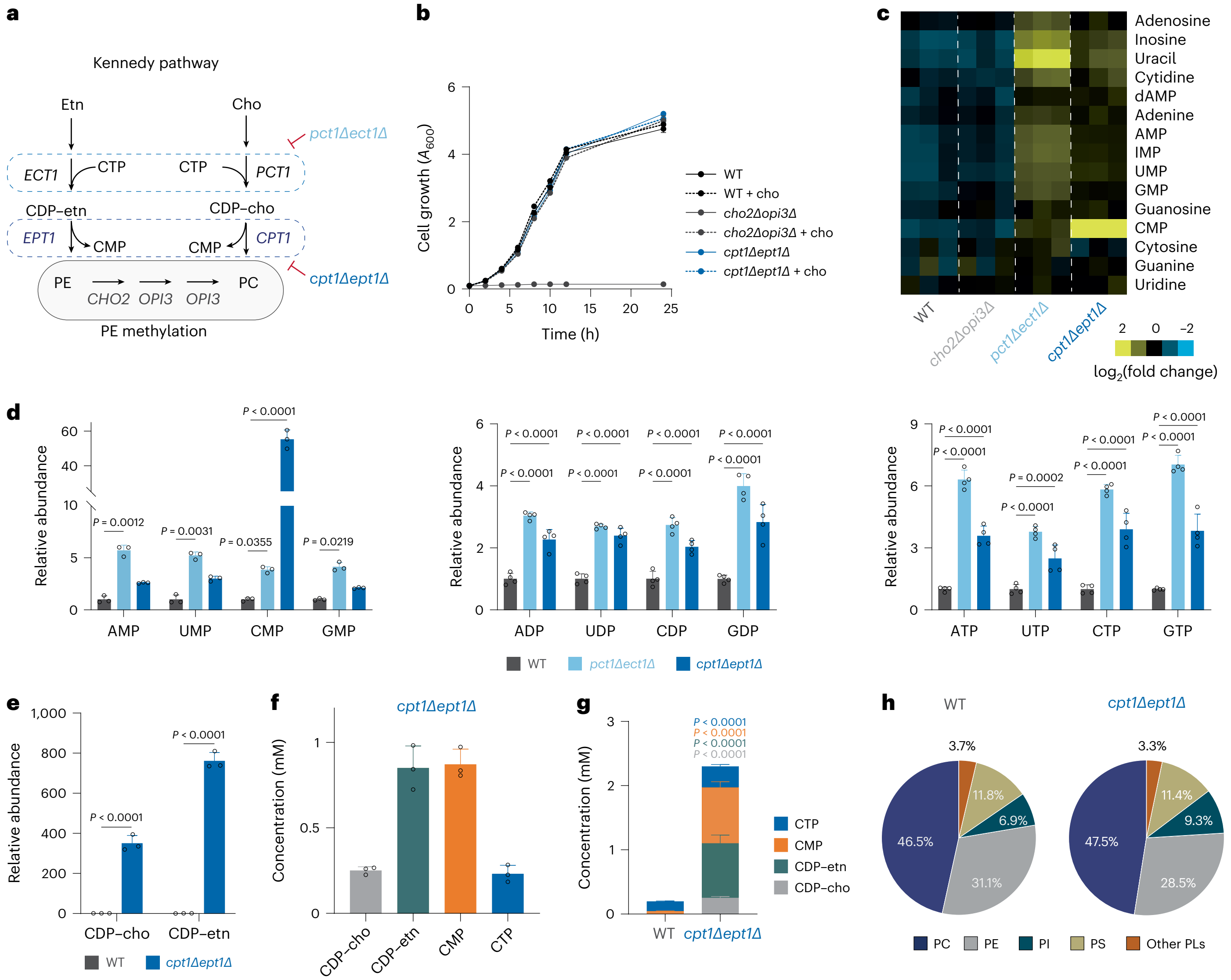

Fig. 2 | The Kennedy pathway is required for maintaining nucleotide homeostasis. **a**, Illustration of pathways involving genes for PE and PC biosynthesis in *S. cerevisiae*. **b**, Growth curves of WT, *cho2Δopi3Δ* and *cpt1Δept1Δ* cells in minimal medium with or without 1 mM choline addition. Data are represented as mean ± s.d. (*n* = 3 biologically independent samples). **c**, Heatmap depicting abundances of nucleotide metabolites in WT, *cho2Δopi3Δ*, *pct1Δect1Δ* and *cpt1Δept1Δ* cells in the log phase. **d**, Relative abundance of nucleoside monophosphates (NMPs, left), nucleoside diphosphates (NDPs, middle) and NTPs (right) in WT, *pct1Δect1Δ* and *cpt1Δept1Δ* cells in the log phase. Data are presented as mean ± s.d. (*n* = 3 biologically independent samples). **e**, Relative abundance of CDP–choline and CDP–ethanolamine in WT and *cpt1Δept1Δ* cells. Data are presented as mean ± s.d. (*n* = 3 biologically independent samples). **f**, Cellular concentrations of CDP–choline, CDP–ethanolamine, CMP and CTP in the *cpt1Δept1Δ* mutant growing logarithmically in minimal medium. **g**, Comparison of cellular concentrations of cytosine-containing nucleotides in WT and the *cpt1Δept1Δ* mutant. Data are presented as mean ± s.d. (*n* = 3 biologically independent samples). **h**, Pie chart depicting compositions of phospholipid classes in WT and *cpt1Δept1Δ* cells growing in the log phase in minimal medium. Source data are provided as a source data file.

3-phosphate from glycolysis (Extended Data Fig. 3g) in both Kennedy pathway-deficient mutants. This indicates a more active carbon flux in the PPP and glycolysis pathways[35].

We further examined the incorporation of newly synthesized nucleotides into RNA by switching WT and mutant cells to a ^{15}N tracing medium containing ^{15}N-ammonium sulfate (Extended Data Fig. 3h). Within 4 h of tracing, RNA bases were gradually replaced by their ^{15}N-labeled counterparts (Extended Data Fig. 3i). Disruption of *CPT1* and *EPT1* delayed the turnover of cytidine in RNA (Extended Data Fig. 3i), highlighting the role of the Kennedy pathway in modulating pyrimidine metabolism.

Kennedy pathway deficiency enhances the reductive capacity

Given that PPP is the major source of NADPH synthesis, we investigated whether the accelerated PPP in Kennedy pathway-deficient mutants would influence the production of cellular-reducing equivalents. Intriguingly, mutants with Kennedy pathway deficiencies exhibited elevated levels of major cellular-reducing equivalents (Fig. 3a–c). Blocking the Kennedy pathway with either *pct1Δect1Δ* or *cpt1Δept1Δ* substantially increased GSH and NADPH levels (Fig. 3a,c). While GSH/oxidized GSH (GSSG) and NADH/NAD$^+$ ratios were similar between WT and the mutants, NADPH/NADP$^+$ ratios were upregulated in the mutants (Fig. 3a–c). Therefore, Kennedy pathway deficiencies enhance NADPH generation, likely attributed to increased PPP flux. Consistently, PPP metabolites R5P, S7P and E4P were substantially increased in the Kennedy pathway-deficient mutants (Fig. 3d).

Epistasis analysis with mutants disrupting the oxidative (*zwf1Δ*) and nonoxidative (*rpe1Δ*) phases of the PPP further supported this idea. Blocking the oxidative phase by *zwf1Δ* predominantly inhibited cell

https://doi.org/10.1038/s41589-024-01689-z

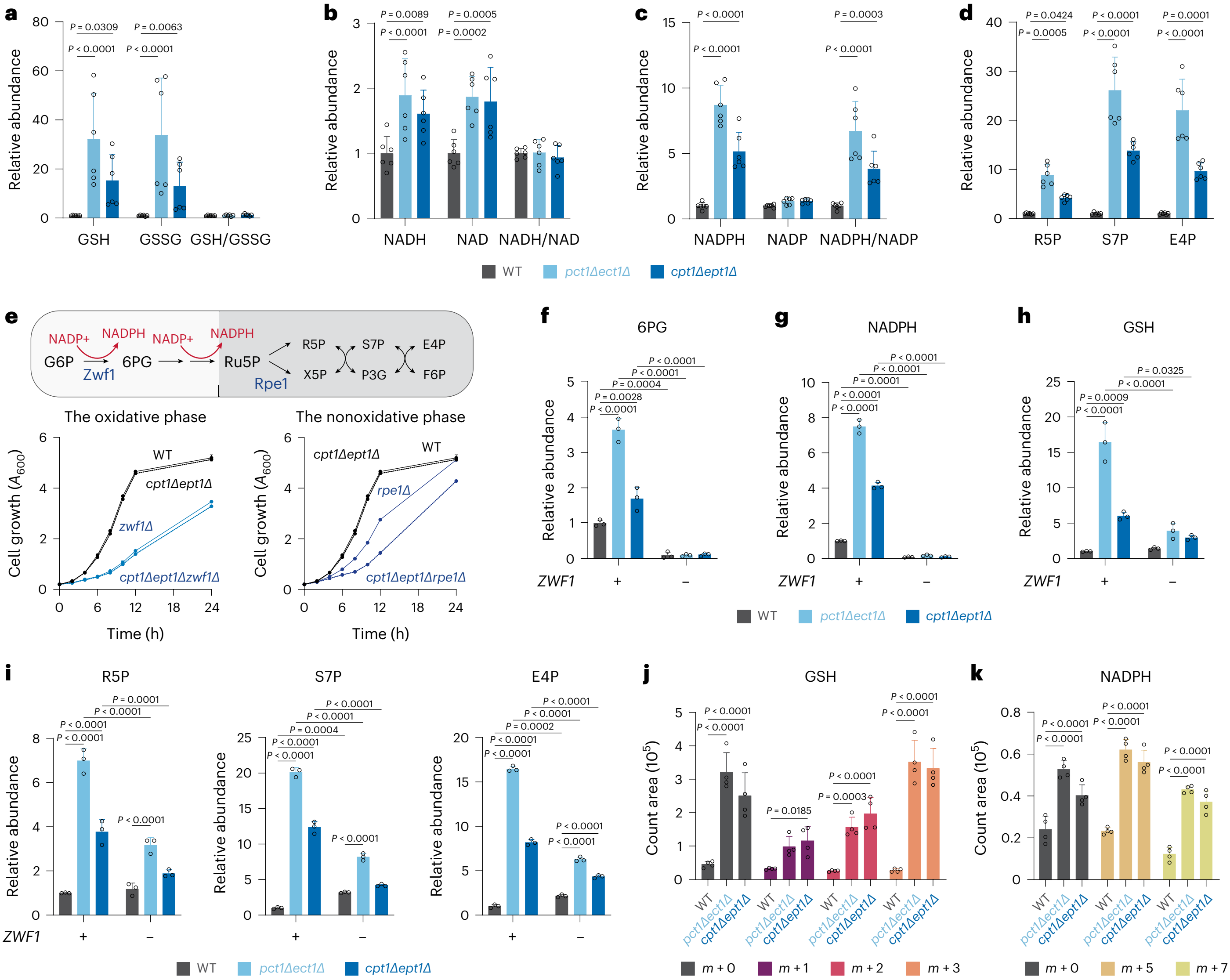

Fig. 3 | A detour from the Kennedy pathway to PE methylation enhances cellular reductive capacity. **a**–**d**, Relative abundance of GSH, GSSG and GSH/GSSG ratio (**a**), NADH, NAD$^+$ and NADH/NAD$^+$ ratio (**b**), NADPH, NADP$^+$ and NADPH/NADP$^+$ ratio (**c**) and PPP metabolites R5P, S7P and E4P (**d**) in WT, *pct1Δect1Δ* and *cpt1Δept1Δ* cells. Data are presented as mean ± s.d. (n = 6 biologically independent samples). **e**, Schematic representation of the PPP and growth curves of WT and indicated mutants in minimal medium. Data are presented as mean ± s.d. (n = 3 biologically independent samples). **f**–**h**, Relative abundance of 6PG (**f**), NADPH (**g**) and GSH (**h**) in WT, *pct1Δect1Δ*, *cpt1Δept1Δ*, *zwf1Δ*, *pct1Δect1Δzwf1Δ* and *cpt1Δept1Δzwf1Δ* cells. Data are presented as mean ± s.d. (n = 3 biologically independent samples). **i**, Relative abundance of R5P, S7P and E4P in WT, *pct1Δect1Δ*, *cpt1Δept1Δ*, *zwf1Δ*, *pct1Δect1Δzwf1Δ* and *cpt1Δept1Δzwf1Δ* cells. Data are presented as mean ± s.d. (n = 3 biologically independent samples). **j**,**k**, Levels of ^{15}N-labeled GSH (**j**) and NADPH (**k**) in WT, *pct1Δect1Δ* and *cpt1Δept1Δ* mutant after tracing with ($^{15}NH_4$)$_2SO_4$ for 60 min. Data are represented as mean ± s.d. (n = 4 biologically independent samples). Source data are provided as a source data file.

growth, while the defective growth of the nonoxidative phase mutant *rpe1Δ* was exacerbated by *cpt1Δept1Δ* (Fig. 3e). This suggests that Kennedy pathway deficiencies induce a metabolic synergy in the PPP to fuel de novo nucleotide synthesis. Next, we conducted a metabolic analysis to confirm these results. As anticipated, *ZWF1* deletion led to a depletion of 6PG and NADPH (Fig. 3f,g), substantially diminishing GSH content (Fig. 3h) and R5P, S7P and E4P levels in Kennedy pathway-deficient mutants (Fig. 3i). Additionally, ^{15}N tracing experiments using a medium with ^{15}N-ammonium sulfate revealed that Kennedy pathway mutants, *pct1Δect1Δ* and *cpt1Δept1Δ*, exhibited substantial increases in newly synthesized GSH and NADPH (Fig. 3j,k). Together, these findings indicate that deficiencies in the Kennedy pathway enhance the cellular production of NADPH and GSH, bolstering reductive capacity. Consistent with this, the Kennedy pathway-deficient mutants displayed increased resistance to H_2O_2 treatment (Extended Data Fig. 4a).

GSH synthesis is stimulated by increased NADPH levels through γ-glutamylcysteine ligase activity[36,37] but is constrained by cysteine availability[17,38], which is not present in a minimal medium. In this medium, devoid of choline, PE methylation is obligatory for PC synthesis. We hypothesized that Kennedy pathway deficiencies hyperactivated PE methylation, using it as a methyl sink for cysteine and GSH synthesis[17,28] (Extended Data Fig. 4b). To test this, we used methionine-(methyl-d3) to label PC from PE methylation and compared newly synthesized PC species ($m + 9$) in WT and the mutant (Extended Data Fig. 4c). The *cpt1Δept1Δ* mutant produced substantially more $m + 9$ PC species, as shown by the top five most abundant PC species (Extended Data Fig. 4d,e). This indicates that Kennedy pathway deficiency is substantially compensated by PE methylation, serving as an active methyl sink fueling GSH synthesis. Thus, disruption of the Kennedy pathway activates pathways for GSH and NADPH production, likely serving as a cell-intrinsic mechanism for modulating antioxidative capacity.

Dysregulated synthesis and turnover cause sharp CMP rises

To further explore how the Kennedy pathway deficiency impacts nucleotide metabolism, we used ^{15}N-ammonium sulfate to trace nucleotide synthesis and turnover in WT and mutant cells (Fig. 4a). Before tracing, steady levels of all NMPs and NTPs were notably elevated in the *cpt1Δept1Δ* mutant (Fig. 4b and Extended Data Fig. 5a,c). Upon switching to the ^{15}N tracing medium, the mutant demonstrated an overall increase in newly synthesized nucleotides labeled with ^{15}N atoms (Fig. 4b and Extended Data Fig. 5a,c). Most nucleotides, including ATP, GTP, UTP, AMP, GMP and UMP, exhibited similar turnover rates in both WT and the *cpt1Δept1Δ* mutant (Extended Data Fig. 5b,d). However, the turnover of CDP–choline and CDP–ethanolamine in the *cpt1Δept1Δ* mutant was relatively slow compared to other nucleotides, likely due to growth dilution (Extended Data Fig. 4f). This finding supports the notion that the AAPT reaction mediated by Cpt1 and Ept1 is the sole pathway consuming these CDP bases.

Blocking the rate-limiting step in the Kennedy pathway by *pct1Δect1Δ* also led to a similar increase in newly synthesized nucleotides as observed in the *cpt1Δept1Δ* mutant (Extended Data Fig. 5e–h). However, evident differences were observed specifically for CMP in the *cpt1Δept1Δ* mutant (Fig. 4b,c). In this mutant, the abundance of fully ^{15}N-labeled CMP ($m + 3$) markedly increased, while the abundance of ^{15}N-labeled CTP and CDP increased moderately (Fig. 4b), supported by the calculated synthesis rate (Extended Data Fig. 4g). The turnover of CMP and cytidine was substantially delayed in the *cpt1Δept1Δ* mutant (Fig. 4c), consistent with notable reductions in their turnover rates (Extended Data Fig. 4h). Furthermore, cytidine-to-CMP ratios, including both steady and labeled levels, showed pronounced decreases in the mutant compared to WT (Fig. 4d,e), indicating a defect in CMP hydrolysis. Thus, unlike other nucleotides, the accumulation of CMP in *cpt1Δept1Δ* cells likely stemmed from increased synthesis and decreased turnover.

CMP hydrolysis enzymes are subject to substrate inhibition

We next focused on understanding why CMP hydrolysis becomes less efficient in the *cpt1Δept1Δ* mutant. We centered our investigation on two nucleotidases, Phm8 and Sdt1, known to hydrolyze NMP into nucleoside and phosphate. In the log phase, Phm8 protein levels dropped by 40–60%, while Sdt1 decreased by 20% in the mutant (Extended Data Fig. 6a–d). Interestingly, stationary phase cells tended to increase Phm8 and decrease Sdt1 protein levels (Extended Data Fig. 6a–d). Phm8 increase in the stationary phase was completely blocked by *cpt1Δept1Δ* (Extended Data Fig. 6a). Despite this, *PHM8* mRNA levels in the mutant increased similarly by more than 100-fold in the stationary phase (Extended Data Fig. 6e), suggesting an unknown post-transcriptional regulation. Similarly, the Sdt1 protein decrease did not correlate with transcription in the stationary phase (Extended Data Fig. 6f). This regulation of Phm8 and Sdt1 implies the dynamic adjustment of nucleotidase activity to metabolic states by modulating enzyme levels.

To understand the regulatory relationship between CMP levels and Phm8 abundance, we overexpressed *PHM8* in both WT and *cpt1Δept1Δ* cells (Extended Data Fig. 6g). While this overexpression did not affect CMP levels in WT cells, it led to a 30% reduction in the mutant (Fig. 4f). However, even with *PHM8* overexpression, CMP levels remained more than 20-fold higher in the mutant than in WT cells (Fig. 4f). In contrast, GMP hydrolysis was highly sensitive to nucleotidase levels. *PHM8* overexpression substantially reduced GMP levels by 60% in WT and 90% in the mutant (Fig. 4f). The inability of increased nucleotidase levels to normalize CMP suggests additional regulatory mechanisms beyond enzyme abundance.

We then characterized Phm8 and Sdt1 enzyme kinetics against various NMPs. Phm8 exhibited stronger catalytic activity for NMP hydrolysis, favoring GMP and CMP (Extended Data Fig. 7a,b), consistent with previous studies[39,40]. Interestingly, both enzymes showed substrate inhibition during CMP hydrolysis (Extended Data Fig. 7c,d). The turning point of maximal activity decreased with lower Phm8 concentrations in vitro (Fig. 4g and Extended Data Fig. 7e). Thus, reduced Phm8 levels likely contribute to the hypersensitivity of CMP hydrolysis to substrate inhibition in the Kennedy pathway-deficient mutant *cpt1Δept1Δ*.

While the turning point at which Phm8 was inhibited remained notably above the cellular CMP concentration in the *cpt1Δept1Δ* mutant, the complex metabolic environment in intact cells prompted us to explore whether the presence of other nucleotide substrates might influence the effective concentrations for inhibiting nucleotide hydrolysis. We evaluated the inhibitory effect of CMP concentration on Phm8 hydrolysis in a reaction system with four substrate NMPs mixed at their reported cellular concentrations[41]. Phm8 could hydrolyze CMP, GMP and UMP at its cellular concentration (10 μg ml^{-1} or 40 nM)[42] (Fig. 4h). Increasing CMP to 1 mM, approximating the intracellular concentration in the *cpt1Δept1Δ* mutant (Fig. 2f), substantially decreased Phm8 nucleotidase activity toward CMP, GMP and UMP (Fig. 4h). This inhibitory effect was evident even at 200 μM of CMP, indicating that substrate inhibition could occur at lower concentrations in the presence of other nucleotides.

We further explored how changes in other NMPs might affect Phm8 activity using this composite mixture. Elevated UMP concentrations markedly inhibited the hydrolysis activity of Phm8 toward CMP, whereas GMP or AMP levels had minimal to no effect (Extended Data Figs. 7f–h). Given the observed increase in all nucleotides in both Kennedy pathway-deficient mutants, we suggest that accumulating pyrimidine nucleotides may induce substrate inhibition, hindering nucleotide salvage while promoting de novo nucleotide synthesis. Thus, CTP usage in the Kennedy pathway establishes a connection between pyrimidine recycling and the regulation of nucleotide biosynthesis and antioxidant production.

Choline enhances NADPH and GSH via CTP trapping in *cpt1Δept1Δ*

Next, we introduced choline, a natural dietary supplement, to a minimal medium at various concentrations to explore its impact on cellular reductive capacity (Fig. 5a). Even without exogenous choline, blocking the Kennedy pathway with *cpt1Δept1Δ* led to substantially elevated levels of choline metabolites, like phosphocholine and CDP–choline (Fig. 5b,c). The addition of 10 μM choline led to a remarkable 460-fold increase in phosphocholine and a 4,300-fold increase in CDP–choline in the mutant, accompanied by a twofold increase in cellular choline levels (Fig. 5a–c). With 1 mM choline, choline, phosphocholine and CDP–choline levels surged to about 30-fold, 1,500-fold and 5,000-fold, respectively (Fig. 5a–c). These substantial increases in CDP–choline levels were expected to siphon cellular CTP, potentially signaling CTP drainage and promoting nucleotide synthesis. In line with this hypothesis, cellular NTP and NMP levels increased with choline supplementation in the *cpt1Δept1Δ* mutant (Fig. 5d–g and Extended Data Fig. 8a–d). This elevated nucleotide demand likely stimulates ribose supply via the PPP, facilitating NADPH generation. Indeed, choline provision enhanced NADPH levels in the *cpt1Δept1Δ* mutant (Fig. 5h), coinciding with a maximal 33-fold increase in GSH levels (Fig. 5i). Unsurprisingly, exogenous choline also heightened the survival rates of the mutant cells under oxidative stress (Fig. 5j). Conversely, the PE methylation-deficient mutant *cho2Δopi3Δ* exhibited hypersensitivity to H_2O_2 in the presence of 1 mM choline (Fig. 5j). These findings suggest that a blockage at the final condensation step in the Kennedy pathway allowed the tuning of cellular reductive capacity based on the availability of choline through the entrapment of CTP in the pyrimidine cache.

As the Kennedy pathway's activity in PC synthesis is affected by the availability of exogenous choline[43], we investigated whether altering

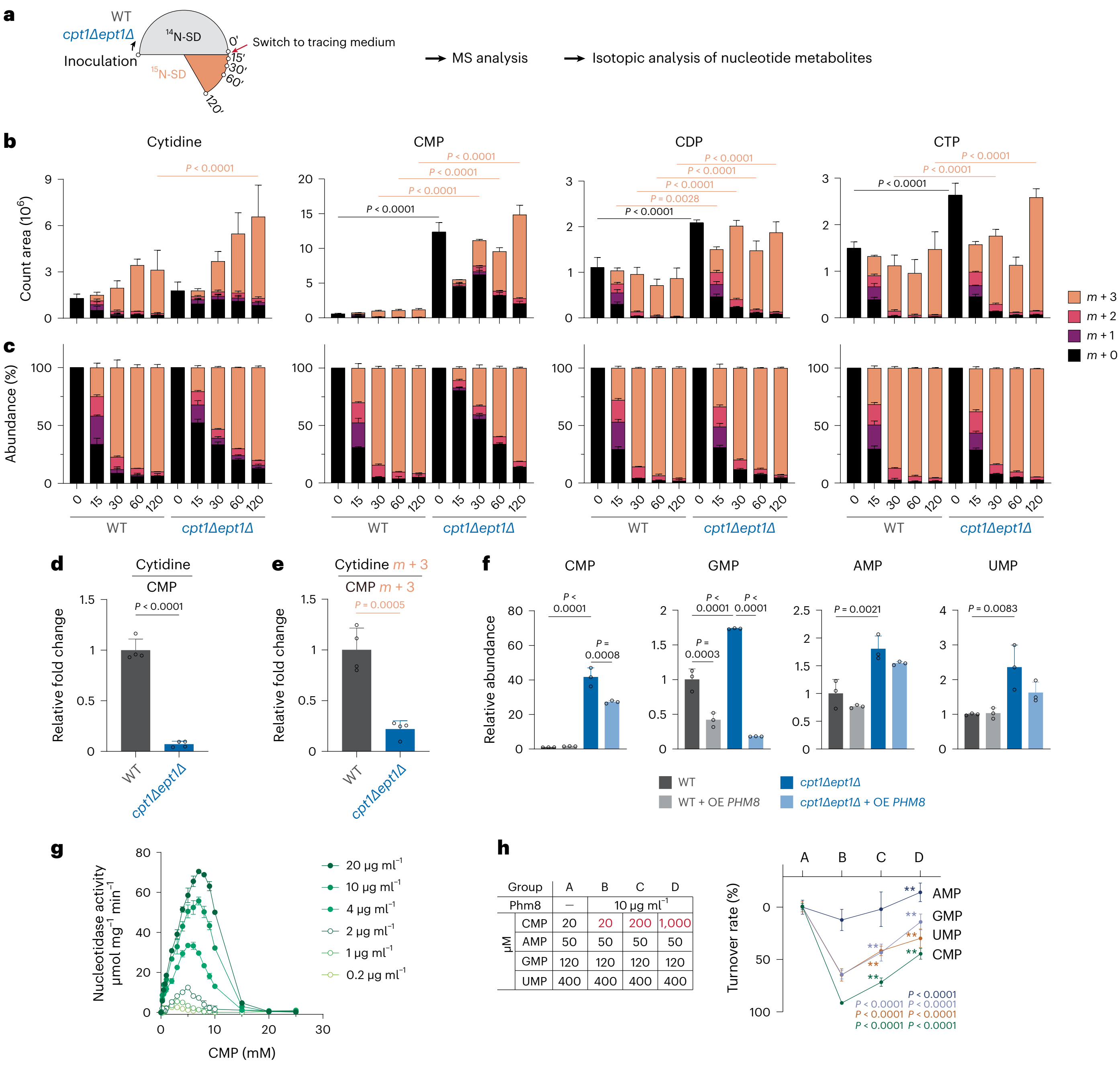

Group	A	B	C	D
Phm8	—	10 μg ml⁻¹		
μM CMP	20	20	200	1,000
AMP	50	50	50	50
GMP	120	120	120	120
UMP	400	400	400	400

Fig. 4 | CMP accumulation uses substrate inhibition to decrease nucleotide salvage upon Kennedy pathway blockage. a, Experimental setup for isotopic tracing of nucleotide metabolism with $(^{15}NH_4)_2SO_4$. **b**, Levels of ^{14}N- and ^{15}N-labeled cytidine, CMP, CDP and CTP in WT and *cpt1Δept1Δ* cells in ^{15}N-SD tracing medium for indicated times. Data are represented as mean ± s.d. ($n = 4$ biologically independent samples). **c**, The percentage abundance of ^{15}N-labeled cytidine, CMP, CDP and CTP in WT and the *cpt1Δept1Δ* mutant in ^{15}N-SD tracing medium for indicated times. Data are represented as mean ± s.d. ($n = 4$ biologically independent samples). **d**,**e**, Relative change in cytidine-to-CMP ratios at steady level (**d**) and fully labeled level (**e**) in WT and *cpt1Δept1Δ* cells 60 min after tracing. Data are represented as mean ± s.d. ($n = 4$ biologically independent samples). **f**, Relative abundances of CMP, GMP, AMP and UMP in WT and the *cpt1Δept1Δ* mutant with or without *PHM8* overexpression. Data are represented as mean ± s.d. ($n = 3$ biologically independent samples). **g**, Phm8 nucleotidase activity curves with enzyme input at different concentrations. Note that CMP substrate concentration for maximal nucleotidase activity decreased with Phm8 concentration. Data are represented as mean ± s.d. ($n = 3$ biologically independent samples). **h**, The turnover rates of CMP, AMP, GMP and UMP in a composite mixture of NMPs. Group A represents a negative control without Phm8; groups B–D represent mixture conditions containing 10 μg ml⁻¹ Phm8 and increasing amounts of CMP. Data are represented as mean ± s.d. ($n = 4$ biologically independent samples). ** denotes statistical significance, with P values indicated in the corresponding colors. Source data are provided as a source data file.

the PC synthesis pathways in response to choline availability impacts nucleotide and antioxidant levels (Extended Data Fig. 8e). Upon choline removal, reductions in cellular choline metabolites (Extended Data Fig. 8f) were observed, accompanied by transient increases in NADPH and GSH levels (Extended Data Fig. 8g,h). However, notable dynamics in nucleotide levels were observed specifically for UMP during this transition (Extended Data Fig. 8i). Given that CMP accumulation occurred in the *cpt1Δept1Δ* mutant (Fig. 2d), it is possible that choline deficiency might disrupt the Kennedy pathway primarily at the rate-limiting step, rather than the terminal step.

https://doi.org/10.1038/s41589-024-01689-z

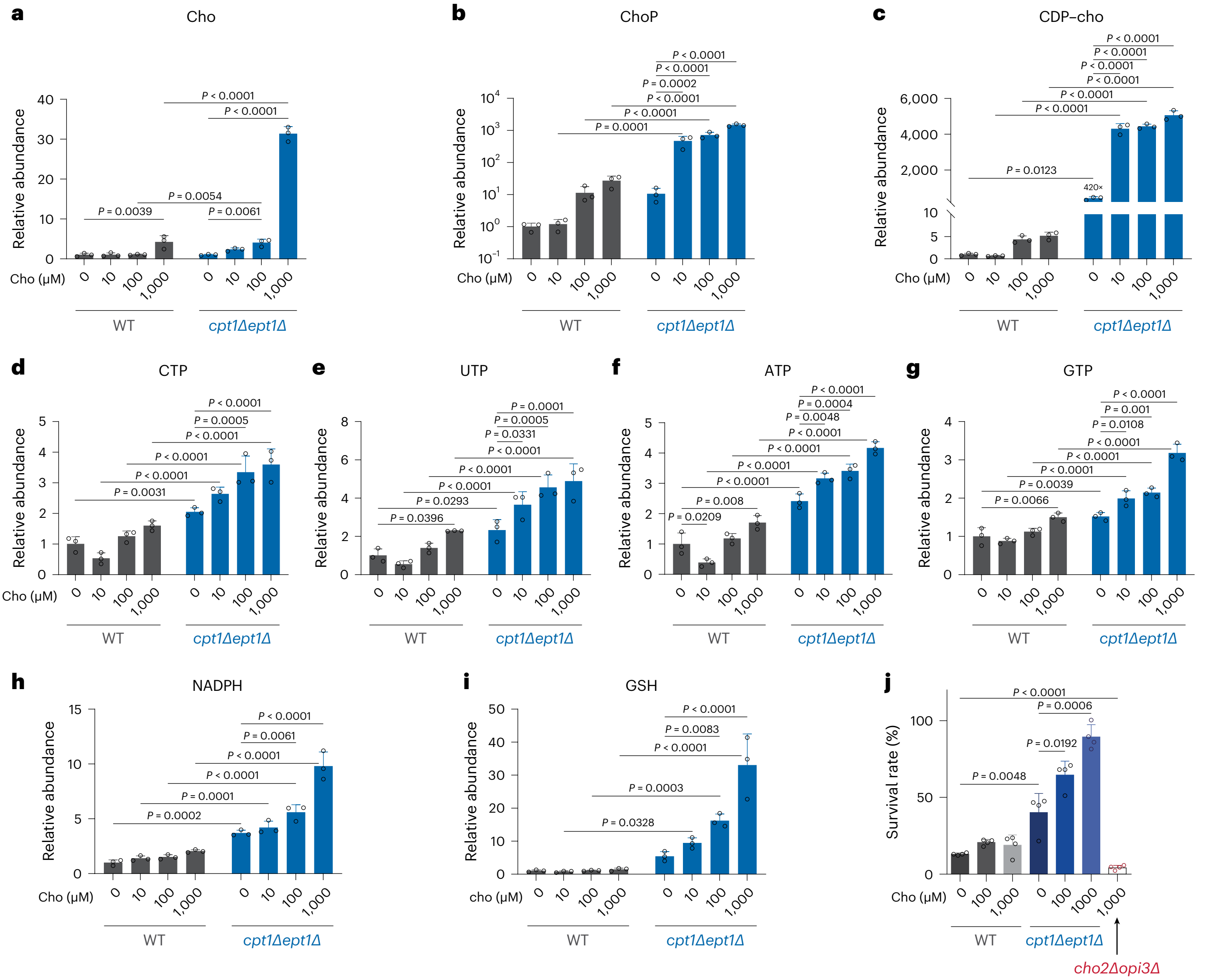

Fig. 5 | Choline enhances cellular reductive capacity by trapping CTP in the pyrimidine cache under Kennedy pathway deficiency. a–**c**, Relative abundance of choline (**a**), phosphocholine (**b**) and CDP–choline (**c**) in WT and *cpt1Δept1Δ* cells in minimal medium with varying choline supplementation. Data are represented as mean ± s.d. (*n* = 3 biologically independent samples). **d**–**g**, Relative abundance of CTP (**d**), UTP (**e**), ATP (**f**) and GTP (**g**) in WT and *cpt1Δept1Δ* cells in minimal medium with different choline supplementation. Data are represented as mean ± s.d. (*n* = 3 biologically independent samples). **h**,**i**, Relative abundance of NADPH (**h**) and GSH (**i**) levels in WT and *cpt1Δept1Δ* cells with different choline supplementation. Data are represented as mean ± s.d. (*n* = 3 biologically independent samples). **j**, Survival rates of WT, *cpt1Δept1Δ* and *cho2Δopi3Δ* cells under H_2O_2 treatment. Cells growing in a minimal medium with indicated amounts of choline provision were subjected to 1 h exposure to 5 mM H_2O_2. Data are represented as mean ± s.d. (*n* = 4 biologically independent samples). Source data are provided as a source data file.

Oxidative stress inhibits the AAPT step in the Kennedy pathway

Having observed an enhanced antioxidative defense upon genetic disruption of the Kennedy pathway, we explored the natural responsiveness of the pathway to oxidative stress. Building on our previous study, which reveals the inhibition of the CDP–choline branch of the Kennedy pathway in an oxidative environment due to histone methylation deficiency[28], we sought to investigate if this responsiveness extended to cells growing in the minimal glucose medium. Under oxidative stress induced by various compounds (Extended Data Fig. 9a), we found increased levels of CDP–choline and CDP–ethanolamine (Extended Data Fig. 9b), indicating inhibition of the Kennedy pathway at the AAPT-mediated condensation step. Consistently, the incorporation of choline-(trimethyl-d9) tracer into PC was blocked under oxidative stress (Extended Data Fig. 9c). Interestingly, AAPT enzymes, Cpt1 and Ept1, formed protein condensates over time during H_2O_2 treatment (Extended Data Fig. 9d), possibly restricting substrate access. These condensates apposed closely to the vacuole marker protein Vph1 and overlapped with the ER marker Sec63-mCherry but not with the processing body (P-body) marker Edc3-mCherry (Extended Data Fig. 9e). Despite unchanged enzyme amounts under H_2O_2 treatment (Extended Data Fig. 9f,g), the formation of these condensates likely limited enzyme activity. Unexpectedly, most DAG species decreased under H_2O_2 treatment (Extended Data Fig. 9h), reducing total DAG levels (Extended Data Fig. 9i). These findings collectively indicate that oxidative stress inhibits the AAPT reaction by limiting DAG availability and restricting substrate access to the enzymes.

To gain further insights into whether oxidative stress directly interferes with the AAPT enzymes, we performed site-directed mutagenesis to alter oxidation-prone cysteine residues in Cpt1 and Ept1. Upon screening all cysteine residues through cysteine-to-serine mutation, we found that *cpt1Δept1Δ* cells expressing either $CPT1^{C98S}$ or $EPT1^{C184S}$

displayed a substantial elevation in CDP–choline or CDP–ethanolamine levels (Extended Data Fig. 10a,b). This finding emphasizes the importance of these residues for enzyme activity. However, these mutations did not prevent protein condensation formed during H_2O_2 treatment (Extended Data Fig. 10c), suggesting that other factors might contribute to this process.

Notably, the formation of AAPT protein condensates occurred gradually, suggesting that the Kennedy pathway may not be the rapid, first-line response to oxidative stress[44–47]. Instead, it might function to restore reductive capacity during recovery from oxidative stress. To investigate this hypothesis, we exposed cells to a 30-min H_2O_2 treatment and switched them to a minimal medium without oxidative stress, monitoring cellular NADPH content. Following the depletion of NADPH in both WT and *cpt1Δept1Δ* cells after the 30-min H_2O_2 treatment (Extended Data Fig. 10d), we observed a subsequent increase in NADPH levels (Extended Data Fig. 10e). Interestingly, the *cpt1Δept1Δ* mutant exhibited a faster increase in NADPH levels after the removal of H_2O_2, followed by an elevation in GSH levels after 2 h (Extended Data Fig. 10e,f). Therefore, cells with a defective Kennedy pathway demonstrated enhanced capacities for restoring cellular reductive capacity after oxidative stress.

Kennedy pathway attenuation for aging antioxidation

As oxidative stress escalates during the aging process[48], we postulate that the activity of the Kennedy pathway may diminish in response to age-associated oxidative stress, thereby acting as a protective mechanism with concurrent antioxidant production. To test this, we used the yeast replicative aging model, isolating aged cells from young cells using a biotin–streptavidin labeling system, as described previously[49] (Fig. 6a). Metabolite analysis revealed a reduction in NADPH and an increase in GSH levels in aged cells, along with substantial increases in $NADP^+$ and GSSG, resulting in profound reductions in both NADPH/$NADP^+$ and GSH/GSSG ratios (Extended Data Fig. 10g,h). This finding confirms increased oxidative stress during replicative aging[50].

Under this oxidative stress, aged cells exhibited an increased fraction of cells with disrupted localization of Cpt1 and Ept1 in the ER (Fig. 6b,c). Consistent with reduced Kennedy pathway activity at the terminal step, the substrate metabolite CDP–choline was elevated by more than 30-fold in aged cells (Fig. 6d). To further substantiate the reduction in Kennedy pathway activity in aged cells, we performed metabolic flux analysis using 100 µM choline (trimethyl-d9) as a tracer (Fig. 6e). Aged cells showed substantial increases in labeled and unlabeled levels of choline metabolites 2 h after the addition of the choline tracer, compared to young cells (Fig. 6f–h). This finding resonates with the observations in the Kennedy pathway mutant *cpt1Δept1Δ* with choline supplementation (Fig. 5a–c), suggesting that aged cells reduced choline usage for PC synthesis in the Kennedy pathway. Consistently, PC synthesis, as estimated by the flux rate, was indeed diminished with age (Fig. 6i). These findings together indicate that the Kennedy pathway for PC synthesis is compromised during replicative aging. To investigate whether the reduction in Kennedy pathway activity contributes to antioxidant production, we compared NADPH and GSH levels in WT and Kennedy pathway-deficient mutant cells with age. Strikingly, blocking the Kennedy pathway at either step was sufficient to elevate NADPH and GSH levels, as well as the ratios of NADPH to $NADP^+$ and GSH to GSSG in aged cells (Fig. 6j,k). Cellular fitness declines with age, as demonstrated by a reduced ability to recover colony growth on a solid plate (Fig. 6l). Coincident with the elevations in antioxidant production, the aged cells with Kennedy pathway deficiency displayed improved fitness (Fig. 6l,m). This finding suggests that the attenuation of Kennedy pathway activity during aging fosters antioxidant production to combat oxidative stress.

Discussion

Here we propose that phospholipid synthesis has evolved as an integrative defense mechanism, requiring coordination with nucleotide metabolism to produce antioxidants. This metabolic connectivity is illustrated as a stepwise, cell-intrinsic flow (Fig. 6n). Oxidative stress inhibits the Kennedy pathway at the AAPT-mediated condensation reaction, leading to the formation of a pyrimidine cache that captures CTP in the form of CDP–choline and CDP–ethanolamine. This oxidative inhibition diverts phospholipid flux away from the Kennedy pathway, resulting in an increase in cellular CMP (Fig. 6n, step 1). Due to substrate inhibition of nucleotidase activity by CMP, the oxidation-induced Kennedy pathway deficiency causes a pronounced increase in CMP (Fig. 6n, step 2). This leads to a reduction in NMP hydrolysis, constraining the salvage pathway and promoting a compensatory activation of de novo nucleotide synthesis and the PPP (Fig. 6n, step 3). The increased flux of the PPP enhances NADPH generation, ultimately stimulating GSH production. Downstream of the CDP–DAG pathway, PE methylation has a crucial role by serving as a methyl sink that synergistically fuels GSH synthesis (Fig. 6n, step 4). As such, alternative pathways for phospholipid synthesis may be activated based on the degree of oxidative stress, representing an automatic control of metabolism that harnesses phospholipid pathways to sense and combat oxidative stress.

CMP accumulation under Kennedy pathway deficiency is a compelling observation, serving as a nodal point connecting the responsive metabolism of phospholipids and nucleotides. Intracellular metabolites, such as CMP, are typically equilibrated at their production and turnover rates. While CMP accumulation can be amplified by substrate inhibition and maintained with decreased nucleotidase protein abundance, it raises the intriguing question of how cellular CMP reaches a critical concentration that restricts nucleotide hydrolysis. This critical concentration may be attributed to the release of CMP from discrete pathways in phospholipid synthesis. As an energy input for phospholipid synthesis, one molecule of CTP is theoretically converted to one molecule of CMP for every phospholipid produced in a cell, irrespective of whether the activated substrates are lipidic or polar metabolites. Increases in CMP were observed to be associated with modest increases in the total amounts of phospholipids in *pah1Δ* and *cpt1Δept1Δ* cells (Extended Data Figs. 1a and 2g). The net increase in phospholipid production may contribute to a net increase in CMP. The synthesis of the phospholipid phosphatidylinositol via CDP–DAG occurs at a very fast rate[51]. The CDP–DAG pathway may generate CMP at a high yield, diffusing from the membranes. This pool of CMP may not be as readily hydrolyzed as the CMP released from CDP-linked polar metabolites in the Kennedy pathway. Thus, reaching an inhibitory CMP level is likely influenced by factors such as the net production of phospholipids, the synthesis rate of CDP–DAG and Kennedy pathways and the spatial concentration and accessibility of CMP to nucleotidase.

Interestingly, the disruption of the Kennedy pathway at the rate-limiting step by *pct1Δect1Δ* also triggers the co-activation of de novo nucleotide synthesis and the PPP, accompanied by an increase in antioxidant production. These common metabolic outcomes highlight that the antioxidative defense mechanism of the Kennedy pathway can be triggered by different environmental cues. Unlike *cpt1Δept1Δ*, the *pct1Δect1Δ* mutant exhibits a generalized increase in most nucleotides, with a notable rise in UMP contributing to the constraint of nucleotide salvage. First, this increase in UMP can reduce Phm8 hydrolysis activity toward CMP. Similar to the pyrimidine cache, this UMP accumulation may ultimately limit NMP hydrolysis and nucleotide recycling (Fig. 6n). Second, during choline deficiency, increases in antioxidant levels coincided with notable dynamics in UMP levels (Extended Data Fig. 8e–i). The increase in UMP likely contributes to the rise in antioxidant production through the inhibition of nucleotide salvage. The rate-limiting step of the Kennedy pathway is highly sensitive to choline availability[43,52,53]. Choline may act as a sentinel metabolite to reflect nutrient status. In its absence, the Kennedy pathway is constrained at the rate-limiting step, reducing CTP usage and leading to enhanced antioxidant production, which is likely crucial for combating stresses associated with nutrient scarcity. However, the specifics of how the regulation of Kennedy

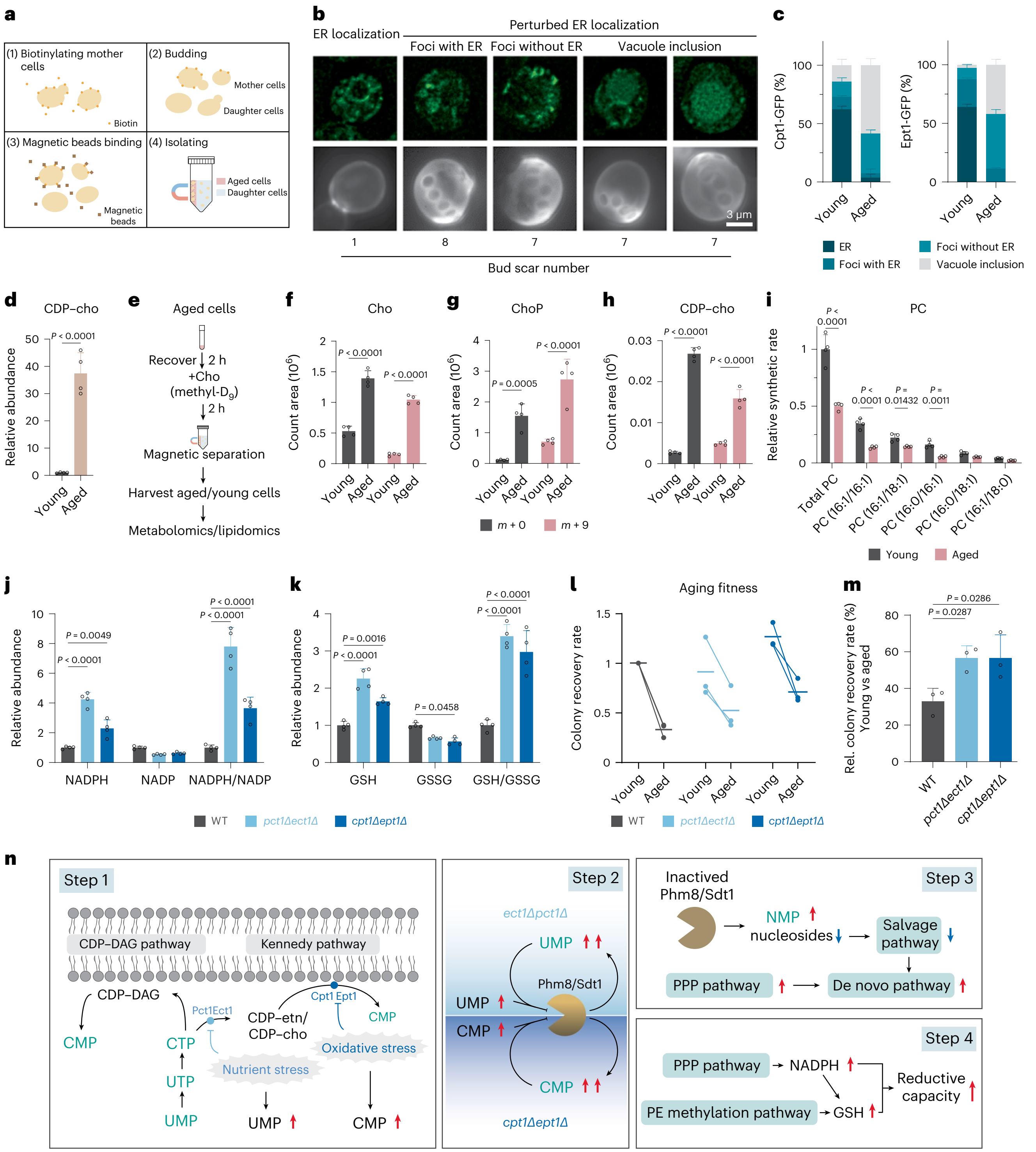

Fig. 6 | Attenuation of Kennedy pathway activity as an antioxidative mechanism during replicative aging. a, Workflow for isolation of aged mother cells and young daughter cells. **b**, Live cell imaging of Cpt1-green-fluorescent protein (GFP) in young and aged cells. The z-projected images show the bud scars. The number of bur scars is noted. **c**, Percentage of young and aged Cpt1-GFP and Ept1-GFP cells with different localization patterns of Cpt1-GFP and Ept1-GFP, including ER, foci with ER, foci without ER and vacuole inclusion. More than 100 cells were counted for each group. Data are presented as mean ± s.d. ($n = 3$ biologically independent samples). **d**, Relative abundance of CDP–choline in aged and young WT cells. Data are presented as mean ± s.d. ($n = 4$ biologically independent samples). **e**, Experimental setup for isotopic tracing of PC synthesis in the Kennedy pathway with choline (trimethyl-d9). **f**–**h**, Levels of labeled choline (**f**), phosphocholine (**g**) and CDP–choline (**h**) in young and aged WT cells. Data are presented as mean ± s.d. ($n = 4$ biologically independent samples). **i**, Relative synthesis rate of PC, indicated by the total PC and the top five most abundant PC species with an $m + 9$ mass shift in young and aged WT cells. The rate for PC synthesis is calculated by normalizing the levels of $m + 9$ labeled PC species to the level of $m + 9$ labeled CDP–choline. Data are presented as mean ± s.d. ($n = 4$ biologically independent samples). **j**,**k**, Relative abundance of NADPH, NADP and NADPH/NADP ratios (**j**) and GSH, GSSG and GSH/GSSG ratios (**k**) in aged WT, *pct1Δect1Δ* and *cpt1Δept1Δ* cells. Data are presented as mean ± s.d. ($n = 4$ biologically independent samples). **l**, Recovery rate of young and aged WT and indicated mutant cells. Data are presented as mean ± s.d. ($n = 3$ biologically independent samples). **m**, Relative recovery rates. Data are presented as mean ± s.d. ($n = 3$ biologically independent samples). **n**, Model illustration. Source data are provided as a source data file.

pathway activity coordinates an increase in CMP or UMP levels remain unknown and await further investigation.

The synthesis of phospholipids is well known to be regulated in response to various growth conditions[54], including growth phase[5], inositol supplementation[55,56] and zinc depletion[57]. Additionally, levels of endogenous precursor metabolites, such as choline[58,59], CTP[60–62] and S-adenosyl methionine (SAM)[63], can influence specific reactions in phospholipid synthesis. Considering the substantial cellular investment in building lipid membranes, it is crucial to recognize that the relationship between phospholipid synthesis and other metabolic processes is bidirectional. For instance, phospholipid methylation consumes substantial amounts of the major methyl donor SAM, facilitating SAM turnover to fuel GSH production[17,28]. Furthermore, the synthesis of highly unsaturated fatty acids[64] and the glycerol-3-phosphate shuttle[65], which provides glycerol backbones for phospholipids, can modulate cellular redox homeostasis by regenerating NAD$^+$. The division of labor for the nucleotide energy carrier CTP in phospholipid synthesis designates an efficient control mechanism for redox homeostasis with this endergonic process. Under the threat of oxidative stress, a safety mechanism regulating the synthesis of phospholipids serves as a critical component in the integrative regulation of nucleotide metabolism, redox balance and membrane biophysical properties for cellular defense.

Online content

Any methods, additional references, Nature Portfolio reporting summaries, source data, extended data, supplementary information, acknowledgements, peer review information; details of author contributions and competing interests; and statements of data and code availability are available at https://doi.org/10.1038/s41589-024-01689-z.

References

1. Parsons, J. B. & Rock, C. O. Bacterial lipids: metabolism and membrane homeostasis. *Prog. Lipid Res.* **52**, 249–276 (2013).
2. Van Meer, G., Voelker, D. R. & Feigenson, G. W. Membrane lipids: where they are and how they behave. *Nat. Rev. Mol. Cell Biol.* **9**, 112–124 (2008).
3. Harayama, T. & Riezman, H. Understanding the diversity of membrane lipid composition. *Nat. Rev. Mol. Cell Biol.* **19**, 281–296 (2018).
4. Vance, J. E. Phospholipid synthesis and transport in mammalian cells. *Traffic* **16**, 1–18 (2014).
5. Carman, G. M. & Henry, S. A. Phospholipid biosynthesis in the yeast *Saccharomyces cerevisiae* and interrelationship with other metabolic processes. *Prog. Lipid Res.* **38**, 361–399 (1999).
6. Vance, J. E. & Vance, D. E. Phospholipid biosynthesis in mammalian cells. *Biochem. Cell Biol.* **82**, 113–128 (2004).
7. Henry, S. A., Kohlwein, S. D. & Carman, G. M. Metabolism and regulation of glycerolipids in the yeast *Saccharomyces cerevisiae*. *Genetics* **190**, 317–349 (2012).
8. Lykidis, A. Comparative genomics and evolution of eukaryotic phospholipid biosynthesis. *Prog. Lipid Res.* **46**, 171–199 (2007).
9. Gibellini, F. & Smith, T. K. The Kennedy pathway—de novo synthesis of phosphatidylethanolamine and phosphatidylcholine. *IUBMB Life* **62**, 414–428 (2010).
10. Dowhan, W., Bogdanov, M. & Eugene, P. Kennedy's legacy: defining bacterial phospholipid pathways and function. *Front. Mol. Biosci.* **8**, 666203 (2021).
11. Kennedy, E. P. & Weiss, S. B. The function of cytidine coenzymes in the biosynthesis of phospholipides. *J. Biol. Chem.* **222**, 193–214 (1956).
12. Henneberry, A. L., Wistow, G. & McMaster, C. R. Cloning, genomic organization, and characterization of a human cholinephosphotransferase. *J. Biol. Chem.* **275**, 29808–29815 (2000).
13. Dowhan, W., Wickner, W. T. & Kennedy, E. P. Purification and properties of phosphatidylserine decarboxylase from *Escherichia coli*. *J. Biol. Chem.* **249**, 3079–3084 (1974).
14. Calzada, E., Onguka, O. & Claypool, S. M. Phosphatidylethanolamine metabolism in health and disease. *Int. Rev. Cell Mol. Biol.* **321**, 29–88 (2016).
15. Acoba, M. G., Senoo, N. & Claypool, S. M. Phospholipid ebb and flow makes mitochondria go. *J. Cell Biol.* **219**, e202003131 (2020).
16. Vance, D. E. & Ridgway, N. D. The methylation of phosphatidylethanolamine. *Prog. Lipid Res.* **27**, 61–79 (1988).
17. Ye, C., Sutter, B. M., Wang, Y., Kuang, Z. & Tu, B. P. A metabolic function for phospholipid and histone methylation. *Mol. Cell* **66**, 180–193 (2017).
18. Cornell, R. B. & Ridgway, N. D. CTP:phosphocholine cytidylyltransferase: function, regulation, and structure of an amphitropic enzyme required for membrane biogenesis. *Prog. Lipid Res.* **59**, 147–171 (2015).
19. Lane, A. N. & Fan, T. W.-M. Regulation of mammalian nucleotide metabolism and biosynthesis. *Nucleic Acids Res.* **43**, 2466–2485 (2015).
20. Vetter, I. R. & Wittinghofer, A. Nucleoside triphosphate-binding proteins: different scaffolds to achieve phosphoryl transfer. *Q. Rev. Biophys.* **32**, 1–56 (1999).
21. Santos-Rosa, H., Leung, J., Grimsey, N., Peak-Chew, S. & Siniossoglou, S. The yeast lipin Smp2 couples phospholipid biosynthesis to nuclear membrane growth. *EMBO J.* **24**, 1931–1941 (2005).
22. Han, G.-S., Wu, W.-I. & Carman, G. M. The *Saccharomyces cerevisiae* lipin homolog is a Mg^{2+}-dependent phosphatidate phosphatase enzyme. *J. Biol. Chem.* **281**, 9210–9218 (2006).
23. Rashid, T. et al. Lipin1 deficiency causes sarcoplasmic reticulum stress and chaperone-responsive myopathy. *EMBO J.* **38**, e99576 (2019).
24. Pascual, F., Soto-Cardalda, A. & Carman, G. M. PAH1-encoded phosphatidate phosphatase plays a role in the growth phase- and inositol-mediated regulation of lipid synthesis in *Saccharomyces cerevisiae*. *J. Biol. Chem.* **288**, 35781–35792 (2013).
25. Park, Y., Han, G.-S., Mileykovskaya, E., Garrett, T. A. & Carman, G. M. Altered lipid synthesis by lack of yeast Pah1 phosphatidate phosphatase reduces chronological life span. *J. Biol. Chem.* **290**, 25382–25394 (2015).
26. Jamil, H., Utal, A. K. & Vance, D. E. Evidence that cyclic AMP-induced inhibition of phosphatidylcholine biosynthesis is caused by a decrease in cellular diacylglycerol levels in cultured rat hepatocytes. *J. Biol. Chem.* **267**, 1752–1760 (1992).
27. Bahmanyar, S. et al. Spatial control of phospholipid flux restricts endoplasmic reticulum sheet formation to allow nuclear envelope breakdown. *Genes Dev.* **28**, 121–126 (2014).
28. Fang, W., Zhu, Y., Yang, S., Tong, X. & Ye, C. Reciprocal regulation of phosphatidylcholine synthesis and H3K36 methylation programs metabolic adaptation. *Cell Rep.* **39**, 110672 (2022).
29. McMaster, C. R. & Bell, R. M. CDP-ethanolamine:1,2-diacylglycerol ethanolaminephosphotransferase. *Biochim. Biophys. Acta* **1348**, 117–123 (1997).
30. Boumann, H. A., de Kruijff, B., Heck, A. J. & de Kroon, A. I. The selective utilization of substrates in vivo by the phosphatidylethanolamine and phosphatidylcholine biosynthetic enzymes Ept1p and Cpt1p in yeast. *FEBS Lett.* **569**, 173–177 (2004).
31. Horibata, Y. & Hirabayashi, Y. Identification and characterization of human ethanolaminephosphotransferase1. *J. Lipid Res.* **48**, 503–508 (2007).
32. Janmey, P. A. & Kinnunen, P. K. J. Biophysical properties of lipids and dynamic membranes. *Trends Cell Biol.* **16**, 538–546 (2006).

33. Bloom, M., Evans, E. & Mouritsen, O. G. Physical properties of the fluid lipid-bilayer component of cell membranes: a perspective. *Q. Rev. Biophys.* **24**, 293–397 (1991).
34. Renne, M. F. & de Kroon, A. I. The role of phospholipid molecular species in determining the physical properties of yeast membranes. *FEBS Lett.* **592**, 1330–1345 (2017).
35. Jang, C., Chen, L. & Rabinowitz, J. D. Metabolomics and isotope tracing. *Cell* **173**, 822–837 (2018).
36. Toroser, D., Yarian, C. S., Orr, W. C. & Sohal, R. S. Mechanisms of γ-glutamylcysteine ligase regulation. *Biochim. Biophys. Acta* **1760**, 233–244 (2006).
37. Olin-Sandoval, V. et al. Lysine harvesting is an antioxidant strategy and triggers underground polyamine metabolism. *Nature* **572**, 249–253 (2019).
38. Walsh, C. T., Tu, B. P. & Tang, Y. Eight kinetically stable but thermodynamically activated molecules that power cell metabolism. *Chem. Rev.* **118**, 1460–1494 (2017).
39. Nakanishi, T. & Sekimizu, K. SDT1/SSM1, a multicopy suppressor of S-II null mutant, encodes a novel pyrimidine 5′-nucleotidase. *J. Biol. Chem.* **277**, 22103–22106 (2002).
40. Xu, Y.-F. et al. Nucleotide degradation and ribose salvage in yeast. *Mol. Syst. Biol.* **9**, 665 (2013).
41. Ljungdahl, P. O. & Daignan-Fornier, B. Regulation of amino acid, nucleotide, and phosphate metabolism in *Saccharomyces cerevisiae*. *Genetics* **190**, 885–929 (2012).
42. Ho, B., Baryshnikova, A. & Brown, G. W. Unification of protein abundance datasets yields a quantitative *Saccharomyces cerevisiae* proteome. *Cell Syst.* **6**, 192–205 (2018).
43. Haider, A. et al. PCYT1A regulates phosphatidylcholine homeostasis from the inner nuclear membrane in response to membrane stored curvature elastic stress. *Dev. Cell* **45**, 481–495 (2018).
44. Kuehne, A. et al. Acute activation of oxidative pentose phosphate pathway as first-line response to oxidative stress in human skin cells. *Mol. Cell* **59**, 359–371 (2015).
45. Reest, J., van der Lilla, S., Zheng, L., Zanivan, S. & Gottlieb, E. Proteome-wide analysis of cysteine oxidation reveals metabolic sensitivity to redox stress. *Nat. Commun.* **9**, 1581 (2018).
46. Shenton, D. & Grant, C. M. Protein S-thiolation targets glycolysis and protein synthesis in response to oxidative stress in the yeast *Saccharomyces cerevisiae*. *Biochem. J.* **374**, 513–519 (2003).
47. Stincone, A. et al. The return of metabolism: biochemistry and physiology of the pentose phosphate pathway. *Biol. Rev.* **90**, 927–963 (2014).
48. Harman, D. Free radical theory of aging: an update: increasing the functional life span. *Ann. N. Y. Acad. Sci.* **1067**, 10–21 (2006).
49. Park, P. U., McVey, M. & Guarente, L. Separation of mother and daughter cells. *Methods Enzymol.* **351**, 468–477 (2002).
50. Saretzki, G. & Von Zglinicki, T. Replicative aging, telomeres, and oxidative stress. *Ann. N. Y. Acad. Sci.* **959**, 24–29 (2002).
51. Gaspar, M. L., Aregullin, M. A., Jesch, S. A. & Henry, S. A. Inositol induces a profound alteration in the pattern and rate of synthesis and turnover of membrane lipids in *Saccharomyces cerevisiae*. *J. Biol. Chem.* **281**, 22773–22785 (2006).
52. McMaster, C. R. & Bell, R. M. Phosphatidylcholine biosynthesis in *Saccharomyces cerevisiae*. Regulatory insights from studies employing null and chimeric sn-1,2-diacylglycerol choline- and ethanolaminephosphotransferases. *J. Biol. Chem.* **269**, 28010–28016 (1994).
53. Wang, Y., MacDonald, J. I. S. & Kent, C. Identification of the nuclear localization signal of rat liver CTP:phosphocholine cytidylyltransferase. *J. Biol. Chem.* **270**, 354–360 (1995).
54. Carman, G. M. & Han, G.-S. Regulation of phospholipid synthesis in the yeast *Saccharomyces cerevisiae*. *Annu. Rev. Biochem.* **80**, 859–883 (2011).
55. Loewen, C. J. R. et al. Phospholipid metabolism regulated by a transcription factor sensing phosphatidic acid. *Science* **304**, 1644–1647 (2004).
56. Carman, G. M. & Henry, S. A. Phosphatidic acid plays a central role in the transcriptional regulation of glycerophospholipid synthesis in *Saccharomyces cerevisiae*. *J. Biol. Chem.* **282**, 37293–37297 (2007).
57. Carman, G. M. & Han, G.-S. Regulation of phospholipid synthesis in *Saccharomyces cerevisiae* by zinc depletion. *Biochim. Biophys. Acta* **1771**, 322–330 (2007).
58. Michel, V., Yuan, Z., Ramsubir, S. & Bakovic, M. Choline transport for phospholipid synthesis. *Exp. Biol. Med.* **231**, 490–504 (2006).
59. Kenny, T. C. et al. Integrative genetic analysis identifies FLVCR1 as a plasma-membrane choline transporter in mammals. *Cell Metab.* **35**, 1057–1071 (2023).
60. McDonough, V. M. et al. Regulation of phospholipid biosynthesis in *Saccharomyces cerevisiae* by CTP. *J. Biol. Chem.* **270**, 18774–18780 (1995).
61. Ostrander, D. B., O'Brien, D. J., Gorman, J. A. & Carman, G. M. Effect of CTP synthetase regulation by CTP on phospholipid synthesis in *Saccharomyces cerevisiae*. *J. Biol. Chem.* **273**, 18992–19001 (1998).
62. Kent, C. & Carman, G. M. Interactions among pathways for phosphatidylcholine metabolism, CTP synthesis and secretion through the Golgi apparatus. *Trends Biochem. Sci.* **24**, 146–150 (1999).
63. Tehlivets, O. Homocysteine as a risk factor for atherosclerosis: is its conversion to S-adenosyl-L-homocysteine the key to deregulated lipid metabolism?. *J. Lipids* **2011**, 702853 (2011).
64. Kim, W. et al. Polyunsaturated fatty acid desaturation is a mechanism for glycolytic NAD^+ recycling. *Cell Metab.* **29**, 856–870 (2019).
65. Liu, S. et al. Glycerol-3-phosphate biosynthesis regenerates cytosolic NAD^+ to alleviate mitochondrial disease. *Cell Metab.* **33**, 1974–1987 (2021).

Methods

Yeast strains and media

All yeast strains used in this study are listed in Supplementary Data 1. All strains and genetic manipulations were verified through sequencing and phenotypes. The prototrophic CEN.PK strain background was used in all experiments[66]. Gene deletions were carried out using standard PCR-based strategies to amplify resistance cassettes with appropriate flanking sequences and replace the target gene by homologous recombination[67]. The epitope tags were introduced into the chromosomal loci at the C terminus of targeted genes and confirmed by PCR and western blots. Medium used in this study included SD minimal medium (0.17% yeast nitrogen base without amino acids containing 0.5% ammonium sulfate (Difco), 2% glucose). Tracing media used in this study were SD-^{15}N (0.17% yeast nitrogen base without amino acids containing 0.05% ^{15}N-ammonium sulfate and 2% glucose), SD-^{13}C (0.17% yeast nitrogen base without amino acids containing 0.5% ammonium sulfate and 0.2% (U-^{13}C6) glucose) and SD-methionine-(methyl-d3) (0.17% yeast nitrogen base without amino acids containing 0.5% ammonium sulfate, 2% glucose, 100 µM methionine-(methyl-d3)). All stable isotope tracers were obtained from Cambridge Isotope Laboratories.

Determination of cell growth by absorbance at 600 nm and spotting assay

To determine cell growth rates in liquid medium culture, cell growth was monitored by absorbance reading at 600 nm using a spectrometer from MAPADA (model P6). For spotting, cells precultured in a minimal medium with 1 mM uracil were washed with a fresh SD medium. A total of 3-µl aliquots of a series of tenfold dilutions from 0.5 optical density at 600 nm (OD_{600}) were spotted onto the SD plate with or without 1 mM uracil and incubated at 30 °C for 1 day.

Lipid extraction and quantification

Yeast lipids were extracted with chloroform:methanol (2:1, vol/vol)[68]. Ten OD_{600} units of yeast cells were harvested for lipid extraction. Cell pellets were resuspended in 0.5 ml MS-grade methanol and lysed by bead-beating. Cell pellets and lysates were then transferred to glass tubes. Chloroform and citric acid were used to achieve phase separation. The bottom lipid phase was collected and dried using a vacuum concentrator system (Labconco). The dried lipid extracts were dissolved in a mixed MS-grade solution containing isopropanol, acetonitrile, water (2:1:1) and 17:0 PC, 17:0 PE and 14:0 PS with Lipidomix (Avanti) used as spike-in standards. The redissolved lipid samples were injected for quantitative analysis by LC–MS/MS with a triple quadrupole mass spectrometer (QTRAP 6500 + System; AB SCIEX). For monoacylglycerol (MAG) measurement, we extracted MAG using chloroform:methanol (2:1, vol/vol) without adding citric acid and resuspended dried lipid samples in a mixture of methanol:dichloromethane (1:1, vol/vol) containing 5 mM ammonium acetate. Lipids separated chromatographically on a C18 column (ACQUITY UPLC BEH C18 column, 130 Å, 1.7 µm, 2.1 mm × 50 mm) were followed by quantification using multiple reaction monitoring (MRM) transitions of mass spectrometry in positive mode for neutral lipids such as DAG and in negative mode for phospholipids such as PE and PC. Specifically, LC was programmed as follows: buffer A contains 33.3% methanol, 33.3% acetonitrile, 33.4% water, 5 mM ammonium acetate, and buffer B contains 5 mM ammonium acetate in 100% isopropanol. The flow rate was 0.15 ml min^{-1} using the following method: $T = 0$ min, 20% buffer B; $T = 1$ min, 20% buffer B; $T = 3$ min, 60% buffer B; $T = 13$ min, 98% buffer B; $T = 13.1$ min, 20% buffer B; $T = 16$ min, 20% buffer B. The retention time for each MRM peak was compared to an appropriate standard. The area under each peak was then quantitated using Analyst Software OS v2.0.

Metabolite extraction and quantitation

Intracellular metabolites were extracted using a previously established method[69]. Care was taken to quench cells quickly and maintain metabolites in acid to minimize oxidation. In brief, equal OD units of cells were rapidly quenched to stop metabolism by addition into four volumes of quenching buffer containing 60% methanol and 10 mM tricine (pH 7.4) that was precooled to −40 °C. After holding at −40 °C for 5 min, the cells were spun at 4,000*g* for 3 min at 4 °C, washed with the same buffer and then resuspended in 1 ml extraction buffer containing 75% ethanol and 0.5 mM tricine (pH 7.4). Intracellular metabolites were extracted by incubating at 75 °C for 3 min, followed by chilling on ice for 10 min. The samples were spun at 15,000*g* for 1 min to pellet cell debris, and 0.9 ml of the supernatant was transferred to a new tube. After a second spin at 15,000*g* for 1 min, 0.8 ml of the supernatant was transferred to a new tube. The extracted metabolites in the extraction buffer were dried using a vacuum concentrator system (Labconco) and stored at −80 °C until analysis. The dried metabolite extracts were resuspended in either 60% acetonitrile or 5 mM ammonium acetate for injection according to specific LC methods used below.

Cellular metabolites were quantitated by LC–MS/MS with a triple quadrupole mass spectrometer (QTRAP 6500 + System; AB SCIEX) using previously established methods[17,70]. Briefly, the redissolved metabolites were separated chromatographically on a SeQuant Zic-hydrophilic interaction liquid chromatography (pHILIC) column (5 µm polymer 150 × 2.1 mm; MilliporeSigma) or a C18-based column with polar embedded groups (Synergi 4 µM Fusion-RP, 150 × 2 mm; Phenomenex), using a high-performance LC system (ExionLC AD System) coupled to a triple quadrupole mass spectrometer (QTRAP 6500 + System; AB SCIEX). For targeted metabolomics, we performed a 34-min LC on the pHILIC column at a flow rate of 0.15 ml min^{-1}, with 20 mM ammonium carbonate and 0.1% (vol/vol) ammonium hydroxide as solvent A and 100% acetonitrile as solvent B. The following gradient was used: 80% solvent B for 0.01 min, 20% solvent B for 20 min, 80% solvent B for 20.5 min and 80% solvent B for 34 min. Metabolites were detected by MRM transitions in positive and negative modes.

For a better separation of nucleotides, we used another LC method using the C18 column. Specifically, we performed a 24-min run at a flow rate of 0.3 ml min^{-1}. In total, 5 mM ammonium acetate in 100% water was used as solvent A and 100% acetonitrile was used as solvent B. The following gradient elution was performed: 0% solvent B for 0.01 min, 0% solvent B for 3 min, 0.2% solvent B for 4 min, 2% solvent B for 5 min, 4% solvent B for 6 min, 6% solvent B for 7 min, 25% solvent B for 11 min, 50% solvent B for 13 min, 100% solvent B for 15 min, 100% solvent B for 18 min, 0% solvent B for 19 min and 0% solvent B for 24 min. The raw data were analyzed with the software OS v2.0.

RIL to quantify nucleotide concentrations

An overnight culture of *cpt1Δept1Δ* cells in SD-^{15}N medium was diluted with fresh SD-^{15}N medium to 0.05 of OD_{600} and harvested when the OD_{600} reached 1.0. One OD unit of cells was collected for metabolite extraction using an extraction buffer with a mixture of ^{14}N-metabolite standards containing ATP, GTP, UTP, CTP, CMP, CDP–choline and CDP–ethanolamine. Molar concentrations of ^{15}N-incorporated metabolites in a sample were calculated based on the intensity peak areas of the added ^{14}N-metabolite standards. Cellular concentrations of each metabolite in a single yeast cell were calculated based on the incurred dilution rate, the number of yeast cells in one OD_{600} unit (1.5×10^7) and the cell volume of a single yeast cell (3.7×10^{-14} l).

Metabolic flux analysis using (U-^{13}C6) glucose

Metabolic flux analysis using (U-^{13}C6) glucose was based on published methods[71,72]. When the growth reached the log phase, cells were spun down, washed with SD medium without glucose and resuspended in the SD-^{13}C tracing medium where the glucose carbons were all ^{13}C-labeled. The cells were collected at the indicated times, and metabolites were extracted as described above. ^{13}C-metabolites were detected by LC–MS/MS, with the targeted parent and daughter ions specific to the ^{13}C form of the metabolites.

Metabolic flux analysis using ^{15}N-ammonium sulfate

^{15}N-ammonium sulfate-based tracing was based on published methods[28,72]. When the growth reached the log phase, cells were spun down, washed with SD medium without ammonium sulfate and resuspended in the SD-^{15}N tracing medium where the sole nitrogen source of ammonium sulfate was ^{15}N-labeled. The cells were collected at the indicated times, and metabolites were extracted as described above. ^{15}N-metabolites were detected by LC–MS/MS, with the targeted parent and daughter ions specific to the ^{15}N form of the metabolites.

Metabolic flux analysis using (1,2-^{13}C2) glucose

Metabolic flux analysis using (U-^{13}C2) glucose was based on products with unique MRM in glycolysis and PPP. When the growth reached the log phase, cells were harvested by centrifugation, washed with SD medium lacking glucose and resuspended in SD-^{13}C2 tracing medium. At specified time points, cells were collected, and metabolites were extracted according to previously established protocols. ^{13}C-metabolites were detected using LC–MS/MS, with the analysis targeting specific parent and daughter ions indicative of the ^{13}C-labeled metabolites.

Isotopic tracing of PC synthesis in the Kennedy pathway with choline-(trimethyl-d9)

Aged cells after 2-h recovery in SD medium were supplemented with 100 μM choline chloride (trimethyl-d9) for tracing. After 2 h of tracing, aged mother cells and young daughter cells were separated. Phospholipids and metabolites were extracted and analyzed using LC–MS/MS. PC (m + 9) denotes newly synthesized PC from the Kennedy pathway. The quantification focused on the top five most abundant PC species, along with choline and its metabolites in the Kennedy pathway for PC synthesis, providing an overall assessment of PC synthesis in the Kennedy pathway.

For the detection of the Kennedy pathway flux in response to H_2O_2 treatment, log phase cells were exposed to 5 mM H_2O_2 for 1 h. Following treatment, cells were washed with fresh SD medium, and 100 μM choline chloride-(trimethyl-d9) was added for 1 h of tracing.

Isotopic tracing of the PE to PC conversion with methionine-(methyl-d3)

In total, 100 μM methionine-(methyl-d3) was added to WT and *cpt1Δept1Δ* log phase cells for tracing. Phospholipids were extracted and analyzed using LC–MS/MS. PC (m + 9) represents newly synthesized PC from PE via a three-step methylation reaction. We quantified the top five most abundant PC species, indicative of an overall rate of the production of PC via PE methylation.

RNA extraction and real-time quantitative PCR analysis

RNA isolation of yeast cells under different growth conditions was carried out following the manufacturer's manual using the MasterPure yeast RNA purification kit (Epicenter). RNA concentration was determined by absorbance at 260 nm. In total, 1 μg RNA was reverse transcribed to cDNA using the HiScript III First Strand cDNA Synthesis Kit (Vazyme). Real-time PCR was performed in triplicate with the ChamQ SYBR qPCR Master Mix from Vazyme. Transcript levels of genes were normalized to *ACT1*. Primers for *ACT1* are as follows: forward, CACCCTGTTCTTTTGACTGAAG and reverse, AGTAACCACGTTCACTCAAGAT. Primers for PHM8 are as follows: forward, GGCTGTTTACAAACTCGTACAA and reverse, GCAATAGGTTATGCCGTCAAAT. Primers for SDT1 are as follows: forward, ACTACTCTAGGACAGATACGCT and reverse, CACTAATGACAATAGCGCCTTC.

Determination of nucleotide incorporation into RNA using ^{15}N-ammonium sulfate

Log phase cells were spun down and washed with SD medium without ammonium sulfate. The cells were then replaced with SD medium with ^{15}N-ammonium sulfate. Total RNA was extracted and proceeded to digestion by adding an acid buffer (0.1 M NaOAc and 20 mM $ZnCl_2$ (pH 6.8)), RNase A and Nuclease P1. After a 4-h incubation at 37 °C, calf intestinal alkaline phosphatase and snake venom diesterase were added to the reaction system in a basic buffer containing 0.3 M NaOAc (pH 7.8). After an overnight incubation at room temperature, supernatants were collected after 5-min centrifugation at 15,000g at 4 °C. The supernatants were further cleared by centrifugation using Amicon Ultra 0.5 ml centrifugal filters at 15,000g for 45 min at 4 °C. The cleared supernatants were diluted and injected for LC–MS/MS analysis.

Determination of membrane surface order with Laurdan

Yeast cells were grown to the log phase in the SD medium. The cells were collected and spheroplasted with 1 mg ml^{-1} zymolyase in 1 M sorbitol. The spheroplasts were incubated with 1 μM Laurdan at 30 °C for 30 min. The samples were excited at 360 nm using SynergyNEO2 Multiscan Spectrum (Biotek), and fluorescence intensities were measured at 440 nm and 490 nm. The Laurdan generalized polarization (GP) value was calculated by the following formula: $\mathrm{GP} = (I_{440} - I_{490})/(I_{440} - I_{490})$. The background of the Laurdan-containing buffer was subtracted from emission values[72].

Determination of yeast survival rates under H_2O_2 treatment

Yeast cells cultured in the log phase were subjected to 5 mM hydrogen peroxide treatment. To measure cell survival rate, an aliquot of liquid culture cells was taken, diluted and spread on YPD plates for colony formation before and after H_2O_2 treatment. The rate of survival was calculated by the following formula: survival rate (%) = (100 × the number of colonies after treatment × dilution factor)/(number of colonies before treatment × dilution factor).

Fluorescence microscopy

For live cell imaging, logarithmically growing cells with *CPT1* and *EPT1* or mutated *CPT1* and *EPT1* with a single cysteine-to-serine mutation chromosomally GFP-tagged at the C terminus were taken for imaging every 30 min under hydrogen peroxide treatment. All images were taken under a ×100, 1.4 numerical aperture (NA) oil-immersion objective lens with a Deltavision Elite microscope (Applied Precision, GE Healthcare). All images were deconvolved using SoftWoRx software.

After the isolation of aged yeast cells using biotin–streptavidin affinity purification, aged cells with CPT1 and EPT1 chromosomally GFP-tagged at the C terminus were taken for imaging. To image bud scars, cells were stained with Fluorescent Brightener 28 (Sigma) for 10 min, then washed and resuspended for fluorescence microscopy. The z-series of the cells was acquired using 30 z sections with 0.3 μm spacing. Images were processed using ImageJ to acquire maximum projection images.

Nucleotidase protein purification and enzyme assay

The plasmids harboring C-terminally Strep-tagged Phm8 or Sdt1 were transformed into *Escherichia coli* BL21 (DE3) for protein purification[73]. The nucleotidase activity of Phm8 and Sdt1 was performed according to previous methods[39,40]. Briefly, the enzyme assay was conducted in a total 60 μl volume reaction containing 0.1 M Tris–HCl (pH 7.0), 10 mM $MgCl_2$ and 1 mM dithiothreitol (DTT). The reaction was stopped in a developer buffer containing 0.86 N H_2SO_4, 1.4% ascorbic acid and 0.36% ammonium molybdate. Nucleotidase activity was assessed by the amount of phosphate released and measured at the absorbance of 820 nm after incubation at 45 °C for 20 min.

Various substrate concentrations between 0 and 25 mM were used to assay the activity of Phm8 against AMP, GMP, UMP and CMP. Substrate concentrations between 0 and 10 mM were used to assay the activity of Sdt1 against AMP, GMP, UMP and CMP. Of note, Sdt1 did not show nucleotidase activity toward AMP and GMP. The kinetic parameters were calculated by fitting the data to the Michaelis–Menten equation. Note that Phm8 and Sdt1 exhibited great differences in nucleotidase activities toward AMP, GMP, UMP and CMP. Enzyme input for each reaction was thus adjusted accordingly so that the readings in the phosphate assay were kept in the same linear range.

Determination of nucleotidase activity in a composite mixture of NMPs

NMPs were mixed at their cellular concentrations of estimate. CMP levels were titrated at 20, 200 and 1,000 μM to examine the effect of substrate inhibition. Phm8 reaction buffer contains 0.1 M Tris–HCl buffer (pH 7.0), 0.1 mM $MgCl_2$ and 20 μg ml^{-1} purified Phm8 protein. The reaction was kept at 30 °C for 10 min and proceeded to metabolite extraction and quantitation using LC–MS/MS as described above.

Whole yeast cell extract preparation and western blotting

A urea-based protocol was used to lyse yeast cells for western blots. Cells were quenched in 20% trichloroacetic acid on ice for 15 min and washed with acetone. Cell pellets were resuspended in urea buffer containing 50 mM Tris–Cl (pH 7.5), 5 mM EDTA, 6 M urea, 1% SDS, 1 mM PMSF, 2 mM sodium orthovanadate and 50 mM NaF and lysed by bead-beating. After collecting supernatants, protein concentration was determined using the Pierce bicinchoninic acid (BCA) protein assay, and the same amounts of proteins were separated using SDS–PAGE gels. Proteins were transferred to a nitrocellulose membrane or a PVDF membrane and blotted with the corresponding antibodies. Blocking was performed in 5% dry milk/Tris Buffered Saline with Tween 20 (TBST), and antibody incubation was performed in 5% dry milk/TBST. Specifically, mouse anti-FLAG M2 antibody (Sigma, F3165) was used at 1:5,000 dilution, and rabbit anti-G6PDH antibody (Sigma, A9521) was used at 1:5,000 dilution.

Isolation of aged yeast cells using biotin–streptavidin affinity purification

Aged yeast cells were isolated based on affinity methods[49]. Cells were grown in SD medium until reaching OD_{600} of 0.5. Then, five units of yeast cells were washed and resuspended in 1 ml of cold PBS. Separately, 2 mg of sulfo-NHS-LC biotin (Thermo Fisher Scientific) was dissolved in 1 ml PBS at room temperature and immediately added to the cells. The cell suspension was incubated at 4 °C for 2 h with gentle agitation. After biotinylation, the cells were washed, diluted and grown in SD medium for six generations. Following growth, the cells were washed and resuspended in 20 ml of cold PBS, and 200 μl of streptavidin magnetic beads (Beyotime) were added to the cells. The mixture was incubated at 4 °C for 2 h with gentle shaking. The suspension was then subjected to magnetic separation using a magnetic sorter (Beyotime) at 4 °C. After 20 min, the supernatant was aspirated, and 20 ml of cold PBS was added. This magnetic sorting was repeated once more. After removing the supernatant, the beads-bound mother cells were resuspended in 1 ml of cold PBS and transferred to a tube placed in the sorter. After 3 min, the supernatant was removed and 1 ml of cold PBS was added. This washing process was repeated seven times. The remaining cells were resuspended in 2 ml of SD medium and cultured for 4 h to allow for recovery. To separate aged mother cells and young daughter cells, the cells underwent the isolation step twice using the magnetic sorter. The supernatant from the first isolation step was collected as young daughter cells, while the remaining cells were harvested as aged mother cells.

Fitness assessment of aged yeast cells

Aged and young cells were obtained following the procedure described above. Cell counts were determined using a hemocytometer. To assess the fitness of yeast cells in a liquid culture, we determine their ability to form single colonies on a solid yeast-extract-dextrose (YPD) plate. To determine this recovery rate, an aliquot of cells was sampled, diluted appropriately and spread onto YPD plates to allow for colony formation. The recovery rate was calculated using the following formula: recovery rate (%) = (100 × number of colonies × dilution factor)/(average cell count per square × 10^4). To compare the fitness of aged WT, *pct1Δect1Δ* and *cpt1Δept1Δ* cells, the recovery rates were normalized to those of the respective young cells.

Statistics and reproducibility

The normalized abundances of metabolites were log-transformed, centered about the median and clustered by the Spearman rank correlation algorithm using cluster 3. Heat maps were attained by the software Treeview 1.2.0. For KEGG pathway analysis, we used MetaboAnalyst 5.0, a web-based analysis platform[74]. For the statistical test used in this study, we used two-tailed Student's *t* tests in Figs. 2e, 4d,e and 6d,f,g–i and Extended Data Figs. 2d–g,i–k and 4a. We used the one-way analysis of variance (ANOVA) method in Figs. 1g, 2d,g, 3a–d,j–k, 4h, 5j and 6j–k,m and Extended Data Figs. 1c, 2a, 4e,g,h, 6e,f, 7f–h, 8f–i, 9b,h and 10a,b,e,g,h and two-way ANOVA method in Figs. 1h,i, 3f–i, 4b,f and 5a–i and Extended Data Figs. 1a, 3b,e,g, 5a,c,e,g, 6c,d, 8a–d, 9i and 10d for comparisons involving multiple groups, with the false discovery rate approach for the calculation of adjusted PO values. The exact *P* values and sample sizes (*n*) are provided in each figure legend. The experiments shown in Figs. 1c,d,g–i, 2b,d–g, 3a–k, 4b–h, 5a–j, 6b–d,f–m and Extended Data Figs. 1a,c, 2d–l, 3b–e,g, 4a,e,f, 5a–h, 6a–g, 7a–h, 8a–d,f–i, 9b,h,i, 10d,g,h were repeated independently at least three times with similar results.

Reporting summary

Further information on research design is available in the Nature Portfolio Reporting Summary linked to this article.

Data availability

All the data supporting the findings of this study presented in this article are available within the article, Supplementary Information and Source data. In addition, the RNA-sequencing data reported in this publication have been deposited in National Center for Biotechnology Information (NCBI)'s Gene Expression Omnibus (GEO) and are accessible through GEO Series accessions GSE269275 and GSE269277. Source data are provided with this paper.

References

66. Van Dijken, J. P. et al. An interlaboratory comparison of physiological and genetic properties of four *Saccharomyces cerevisiae* strains. *Enzyme Microb. Technol.* **26**, 706–714 (2000).
67. Longtine, M. S. et al. Additional modules for versatile and economical PCR-based gene deletion and modification in *Saccharomyces cerevisiae*. *Yeast* **14**, 953–961 (1998).
68. Yang, S., Xue, J. & Ye, C. Protocol for rapid and accurate quantification of phospholipids in yeast and mammalian systems using LC–MS. *STAR Protoc.* **3**, 101769 (2022).
69. Tu, B. P. et al. Cyclic changes in metabolic state during the life of a yeast cell. *Proc. Natl Acad. Sci. USA* **104**, 16886–16891 (2007).
70. Ye, C. et al. Demethylation of the protein phosphatase PP2A promotes demethylation of histones to enable their function as a methyl group sink. *Mol. Cell* **73**, 1115–1126 (2019).
71. Yuan, M. et al. Ex vivo and in vivo stable isotope labelling of central carbon metabolism and related pathways with analysis by LC–MS/MS. *Nat. Protoc.* **14**, 313–330 (2019).
72. Fang, W. et al. Methionine restriction constrains lipoylation and activates mitochondria for nitrogenic synthesis of amino acids. *Nat. Commun.* **14**, 2504 (2023).
73. Lu, H. et al. Phase-separation mechanism for C-terminal hyperphosphorylation of RNA polymerase II. *Nature* **558**, 318–323 (2018).
74. Xia, J. & Wishart, D. S. Web-based inference of biological patterns, functions and pathways from metabolomic data using MetaboAnalyst. *Nat. Protoc.* **6**, 743–760 (2011).

Acknowledgements

We gratefully acknowledge the Core Facility of the Life Sciences Institute, Zhejiang University, for their support, and special thanks to X. Jiang and Q. Liang (Zhejiang University) for their technical assistance with MS, using the AB SCIEX triple Quad 6500+ and 5500+ systems. This work was supported by grants from the National Key Research and Development Program of China (2023YFA1801100), the National Natural Science Foundation of China (32270816 and 92057102), the Double Thousand Plan of Jiangxi Province (jxsq2023102239), the Fundamental Research Funds for the Central Universities, a research fund from the Zhejiang Provincial Key Laboratory for Cancer Molecular Cell Biology, the startup fund from the Life Sciences Institute of Zhejiang University and the 1000 Talents Program for Young Scholars to C.Y.

Author contributions

C.Y., Y.Z., X.T. and J.X. conceived the study. Y.Z., X.T. and J.X. performed most of the experiments and conducted data analysis. H.Q. assisted with the fluorescence microscopy experiments. C.Y., Z.-C.T., D.Z. and D.-Q.Z. supervised the project. C.Y., X.T., Y.Z. and D.-Q.Z. wrote the manuscript. C.Y. provided the funding.

Competing interests

The authors declare no competing interests.

Additional information

Extended data is available for this paper at https://doi.org/10.1038/s41589-024-01689-z.

Supplementary information The online version contains supplementary material available at https://doi.org/10.1038/s41589-024-01689-z.

Correspondence and requests for materials should be addressed to Cunqi Ye.

Peer review information *Nature Chemical Biology* thanks Neale Ridgway and the other, anonymous, reviewer(s) for their contribution to the peer review of this work.

Reprints and permissions information is available at www.nature.com/reprints.

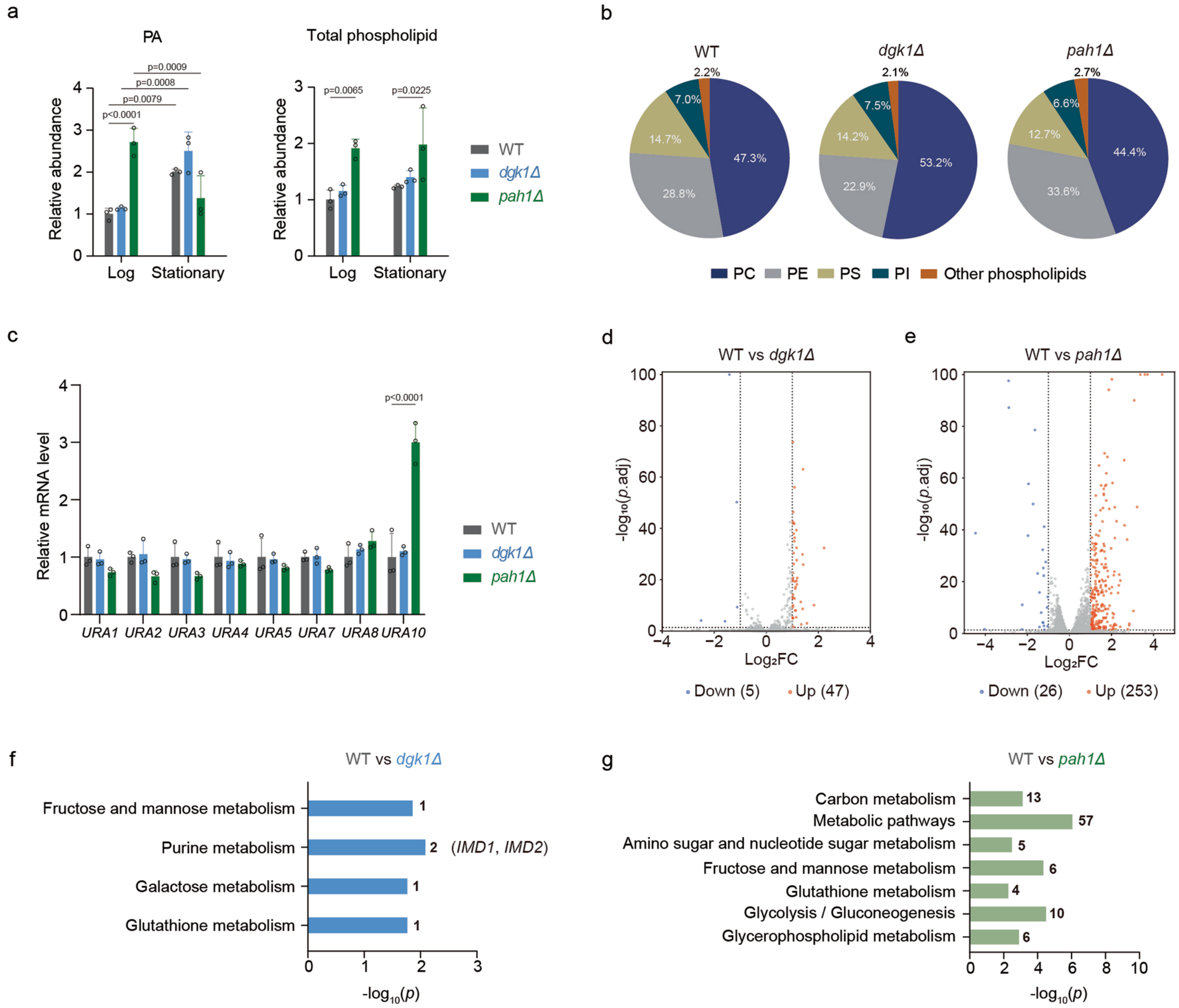

Extended Data Fig. 1 | Coordinated transcriptional regulation of metabolic genes due to dysregulation in PA to DAG conversion. (**a**) Relative abundance of PA and total phospholipids in WT, *dgk1Δ* and *pah1Δ* cells. Data are presented as mean ± SD (n = 3; n = biologically independent samples). (**b**) Pie chart depicting the composition of different phospholipid classes in WT, *dgk1Δ*, and *pah1Δ* cells in the log phase in minimal medium. (**c**) Relative mRNA levels of genes involved in pyrimidine de novo synthesis in WT and *pah1Δ* cells in the log phase in minimal medium. Data are presented as mean ± SD (n = 3; n = biologically independent samples). (**d**,**e**) Volcano plots of significantly differential expression of mRNAs in *dgk1Δ* (**d**) and *pah1Δ* (**e**) cells. (**f**,**g**) Enriched KEGG pathway analysis of significantly differentially expressed genes in *dgk1Δ* (**f**) and *pah1Δ* (**g**).

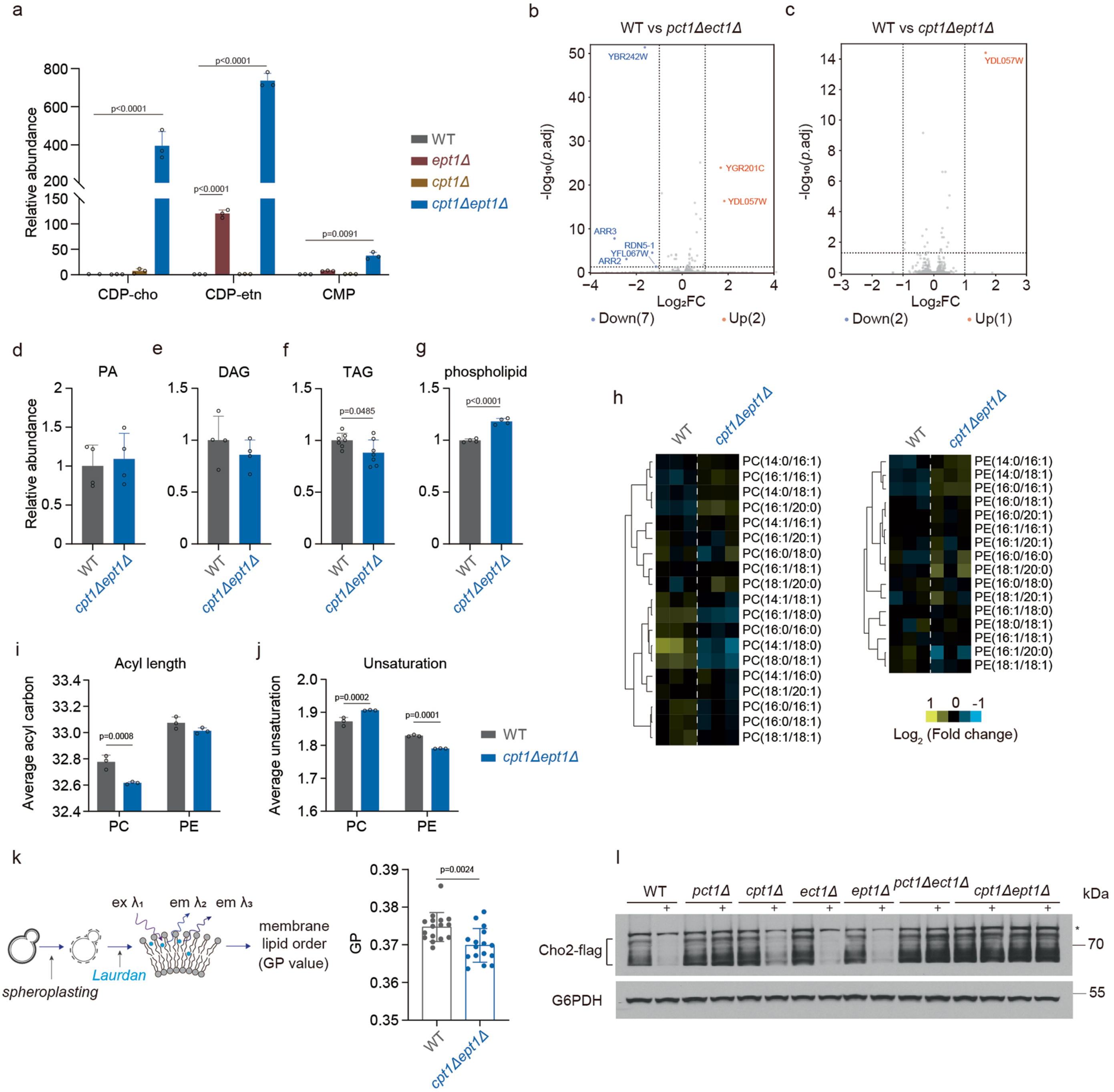

Extended Data Fig. 2 | Kennedy pathway deficiency alters phospholipid composition and membrane order independent of significant transcriptional regulation. (**a**) Relative abundance of CDP-choline (CDP-cho), CDP-ethanolamine (CDP-etn) and CMP in WT and indicated mutants. Data are presented as mean ± SD (n = 3; n = biologically independent samples). (**b**,**c**) Volcano plots showing significantly differential expression of mRNAs in *pct1Δect1Δ* (**b**) and *cpt1Δept1Δ* (**c**) cells. (**d**–**g**) Relative abundance of PA (**d**), DAG (**e**), TAG (**f**) and total phospholipids (**g**) in WT and *cpt1Δept1Δ* cells in the log phase in minimal medium. Data are presented as mean ± SD (**d**,**e**,**g**, n = 4; **f**, n = 7; n = biologically independent samples). (**h**) Heatmap showing abundances of PC and PE species in WT and *cpt1Δept1Δ* cells. (**i**,**j**), Average acyl length (**i**) and unsaturation (**j**) of PC and PE in WT and *cpt1Δept1Δ* cells in the log phase. Data are represented as mean ± SD (n = 4; n = biologically independent samples). (**k**) Membrane order state of spheroplasted cells assayed by the fluorescence spectral shift of Laurdan. Data are expressed as generalized polarization (GP) values and presented as mean ± SD (n = 16; n = biologically independent samples). (**l**) Western blots assaying protein levels of Cho2-flag in WT and indicated mutants harvested in log phases in SD minimal medium with or without choline supplement. G6PDH was used as a loading control. The asterisk (*) denotes a non-specific band. Data are representative of three independent experiments.

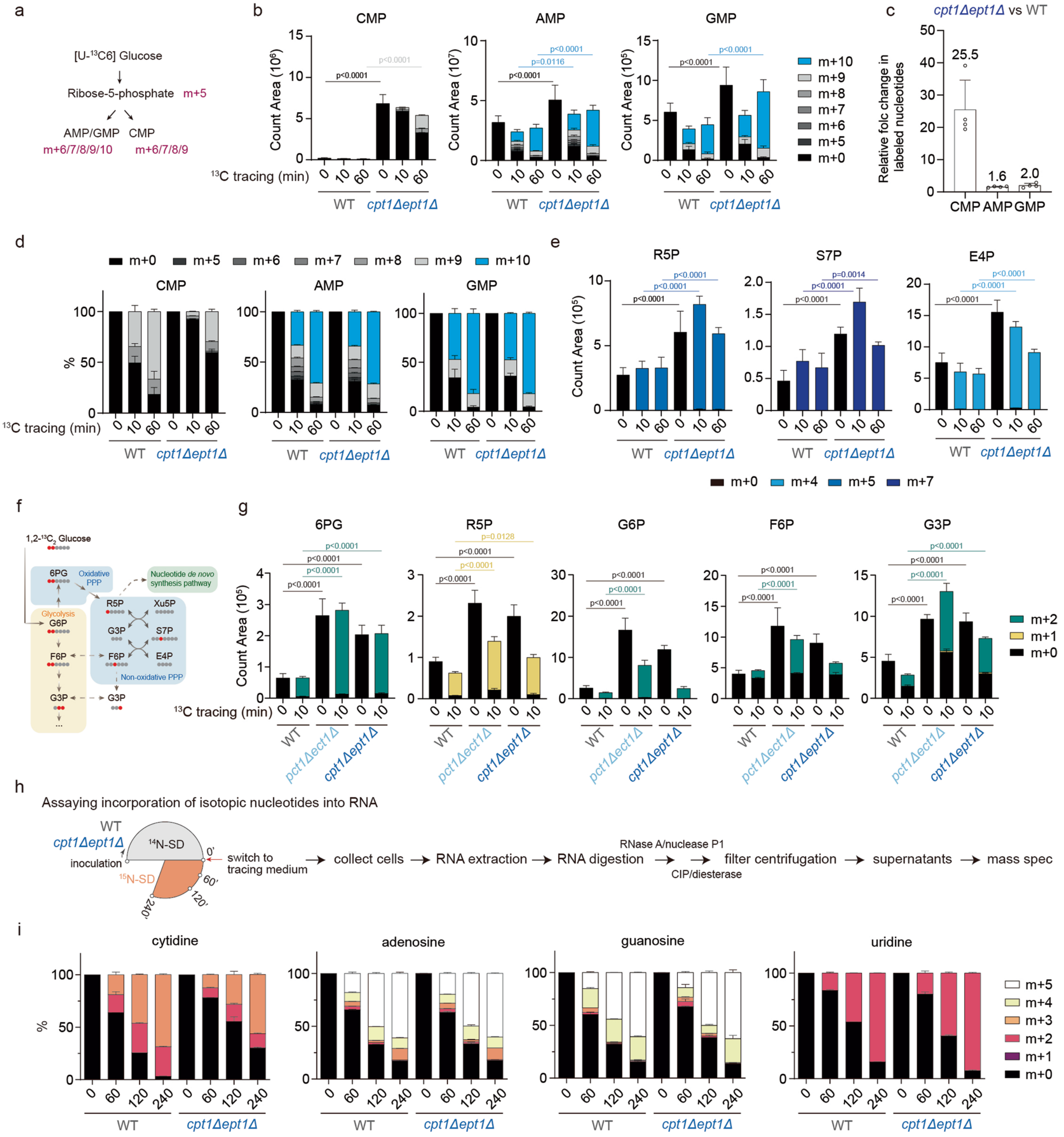

Extended Data Fig. 3 | Kennedy pathway deficiency leads to activation of nucleotide synthesis and the PPP. (**a**) Diagram showing ^{13}C incorporation from [U-^{13}C6] glucose into corresponding nucleotides. (**b**) Levels of ^{13}C-labeled CMP, AMP and GMP in WT and mutant cells after tracing with [U-^{13}C6] glucose. Data are represented as mean ± SD (n = 4; n = biologically independent samples). (**c**) Relative abundance of fully labeled CMP, AMP and GMP in WT and mutant cells after a 60-min tracing with [U-^{13}C6] glucose. (**d**) Percent abundance of ^{13}C-labeled CMP, AMP and GMP in WT and mutant cells after tracing with [U-^{13}C6] glucose. Data are represented as mean ± SD (n = 4; n = biologically independent samples). (**e**) Levels of ^{13}C-labeled R5P, S7P and E4P in WT and the *cpt1Δept1Δ* mutant after tracing with [U-^{13}C6] glucose. Data are represented as mean ± SD (n = 4; n = biologically independent samples). (**f**) Diagram of glycolysis and the PPP with illustration of 1,2-$^{13}C_2$ glucose incorporation into corresponding metabolites. (**g**) Levels of ^{13}C-labeled 6PG, R5P, G6P, F6P and G3P in WT and mutant cells after tracing with [1,2-$^{13}C_2$] glucose. Data are represented as mean ± SD (n = 4; n = biologically independent samples). (**h**) Schematic showing the assay for incorporation of nucleotides into RNA. (**i**) Percent abundance of ^{15}N-labeled cytidine, adenosine, guanosine and uridine released from total RNA in WT and *cpt1Δept1Δ* cells incubated with $(^{15}NH_4)_2SO_4$ tracer.

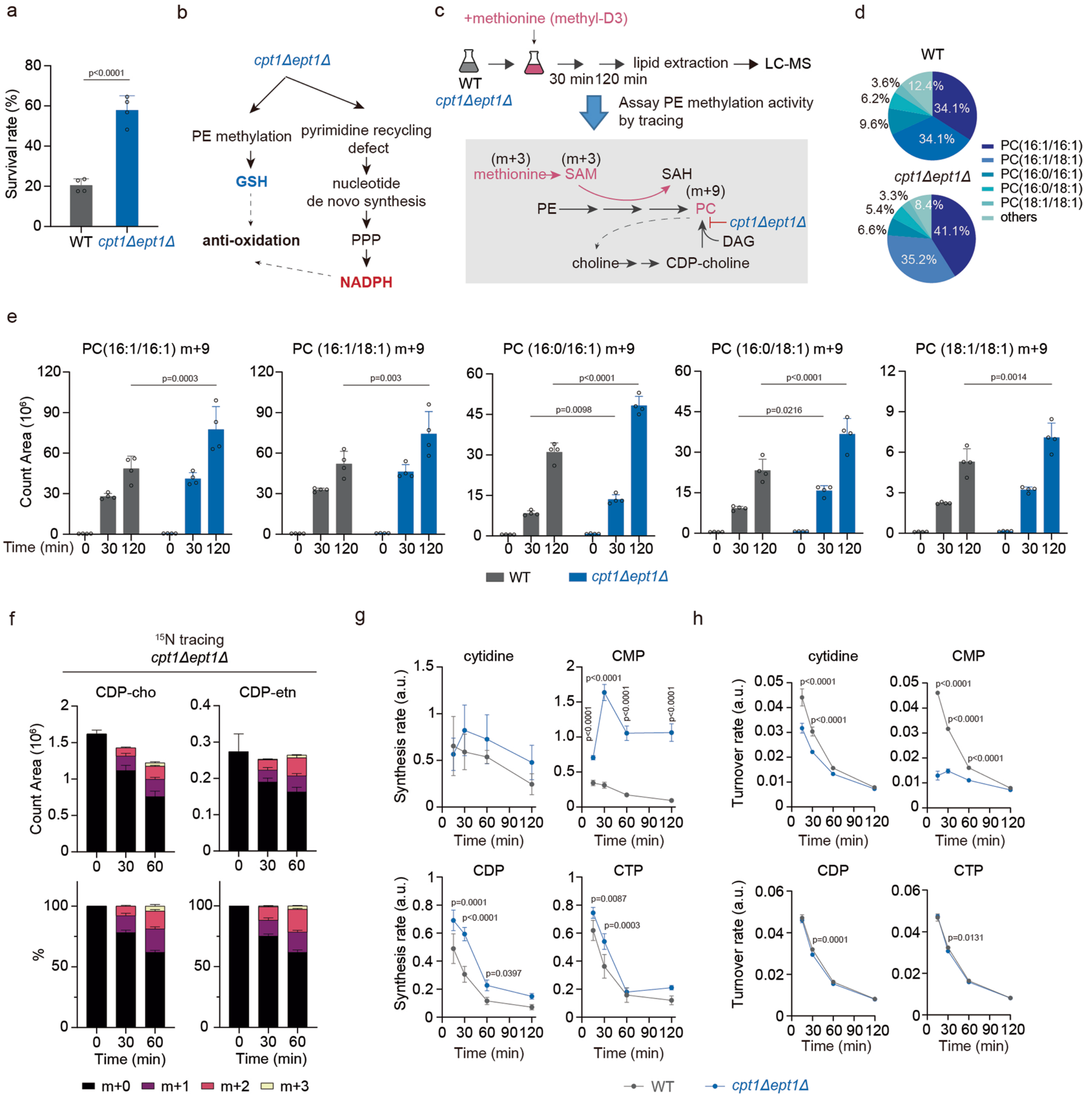

Extended Data Fig. 4 | Kennedy pathway deficiency is compensated by PE methylation that fuels GSH synthesis. (**a**) Survival rate of WT and *cpt1Δept1Δ* cells with a 30-min exposure to 5 mM H_2O_2. (**b**) Diagram illustrating antioxidant pathways that generate reducing equivalents cooperatively. (**c**) Schematic of the assay to determine the rate of PC synthesis from PE methylation using 100 µM methionine-(methyl-d3). (**d**) Pie chart depicting compositions of different PC classes in WT and *cpt1Δept1Δ* cells growing in the log phase in minimal medium. (**e**) Levels of the top 5 most abundant PC species with an m + 9 mass shift in WT and *cpt1Δept1Δ* cells. Note that m + 9 PC is derived from PE via methylation. Data are represented as mean ± SD (n = 4; n = biologically independent samples). (**f**) Levels and percent abundance of ^{15}N-labeled CDP-choline and CDP-ethanolamine in the *cpt1Δept1Δ* mutant after tracing with $(^{15}NH_4)_2SO_4$. Data are represented as mean ± SD (n = 4; n = biologically independent samples). (**g**) Average synthesis rates of newly synthesized cytidine, CMP, CDP and CTP in WT and the *cpt1Δept1Δ* mutant after tracing with $(^{15}NH_4)_2SO_4$. (**h**) Average turnover rates of cytidine, CMP, CDP and CTP in WT and the *cpt1Δept1Δ* mutant after tracing with $(^{15}NH_4)_2SO_4$.

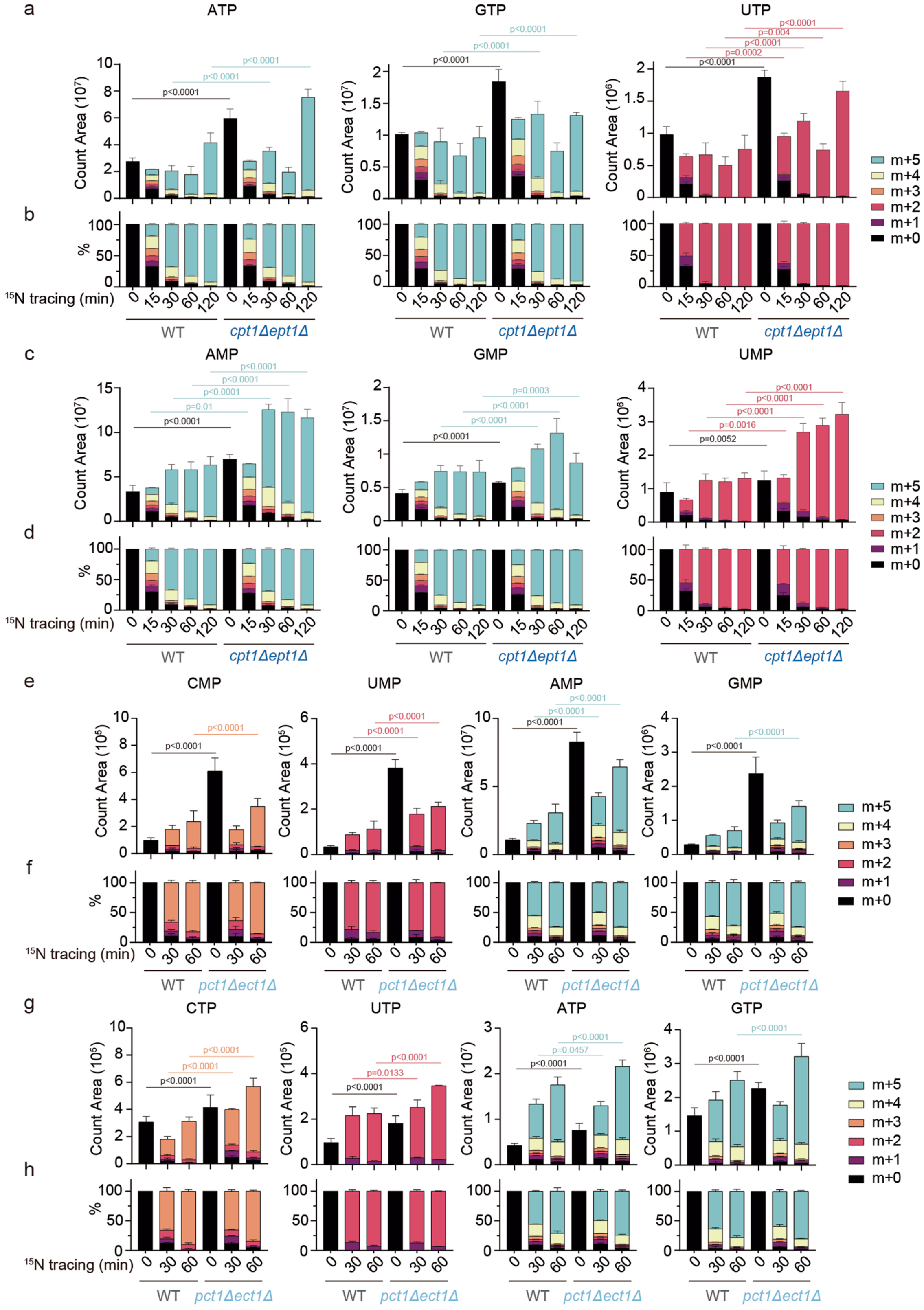

Extended Data Fig. 5 | Synthesis and turnover of nucleotides in Kennedy pathway-deficient mutants. (**a**–**d**) Levels (**a**) and the percent abundance (**b**) of ^{15}N-labeled ATP, GTP and UTP, together with levels (**c**) and the percent abundance (**d**) of ^{15}N-labeled AMP, GMP and UMP in WT and the *cpt1Δept1Δ* mutant after tracing with $(^{15}NH_4)_2SO_4$. Data are represented as mean ± SD (n = 4; n = biologically independent samples). (**e**–**h**) Levels (**e**) and the percent abundance (**f**) of ^{15}N-labeled CMP, UMP, AMP and GMP, together with levels (**g**) and the percent abundance (**h**) of ^{15}N-labeled CTP, UTP, ATP and GTP in WT and the *pct1Δect1Δ* mutant after tracing with $(^{15}NH_4)_2SO_4$. Data are represented as mean ± SD (n = 4; n = biologically independent samples).

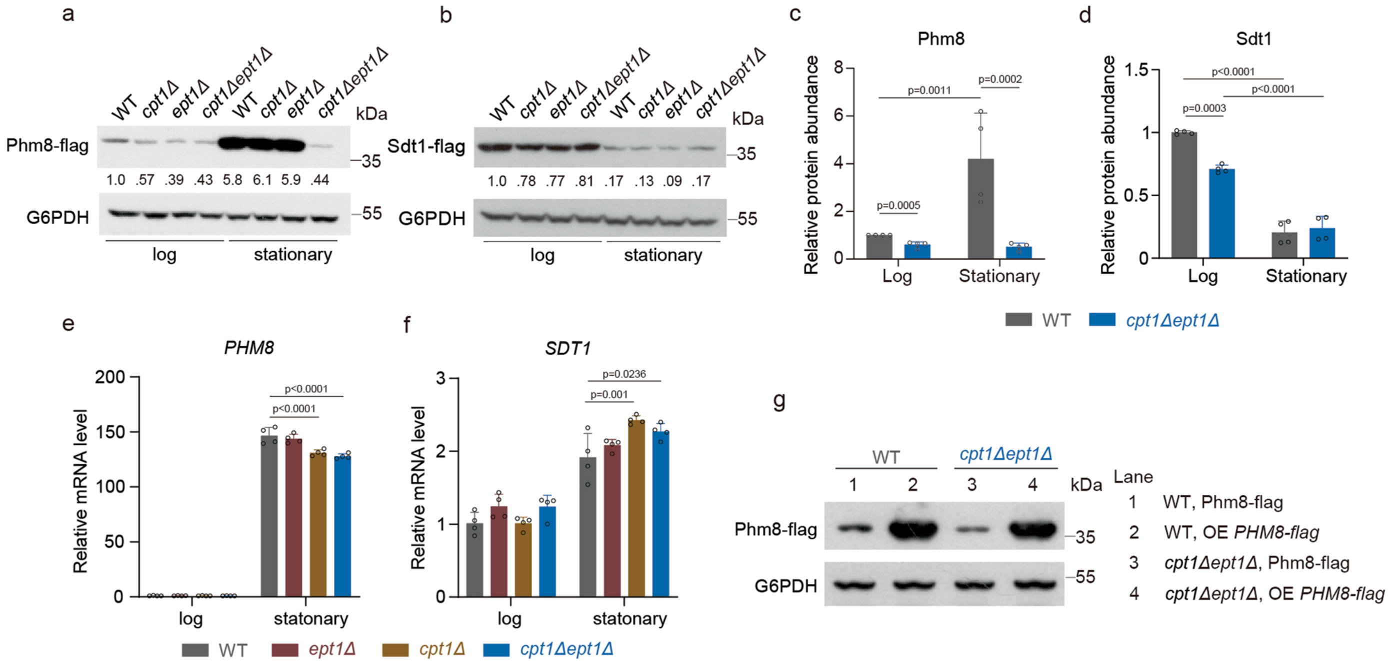

Extended Data Fig. 6 | Protein and transcriptional expression of nucleotidases in WT and *cpt1Δept1Δ* cells. (**a**,**b**) Western blots assaying protein levels of nucleotidases Phm8-flag (**a**) and Sdt1-flag (**b**) in WT, *cpt1Δ*, *ept1Δ* and *cpt1Δept1Δ* cells harvested in log and stationary phases. G6PDH was used as a loading control. Data are representative of at least three independent experiments. (**c**,**d**) Relative protein abundance of Phm8 (**c**) and Sdt1 (**d**) in WT and *cpt1Δept1Δ* cells in log and stationary phases. Data are represented as mean ± SD (n = 4; n = biologically independent samples). (**e**,**f**) Relative mRNA level of *PHM8* (**e**) and *SDT1* (**f**) in WT, *ept1Δ*, *cpt1Δ* and *cpt1ept1Δ* cells in minimal medium at log and stationary phases. Data are represented as mean ± SD (n = 4; n = biologically independent samples). (**g**) Western blots assaying protein levels of nucleotidase Phm8-flag. G6PDH was used as a loading control. Data are representative of three independent experiments.

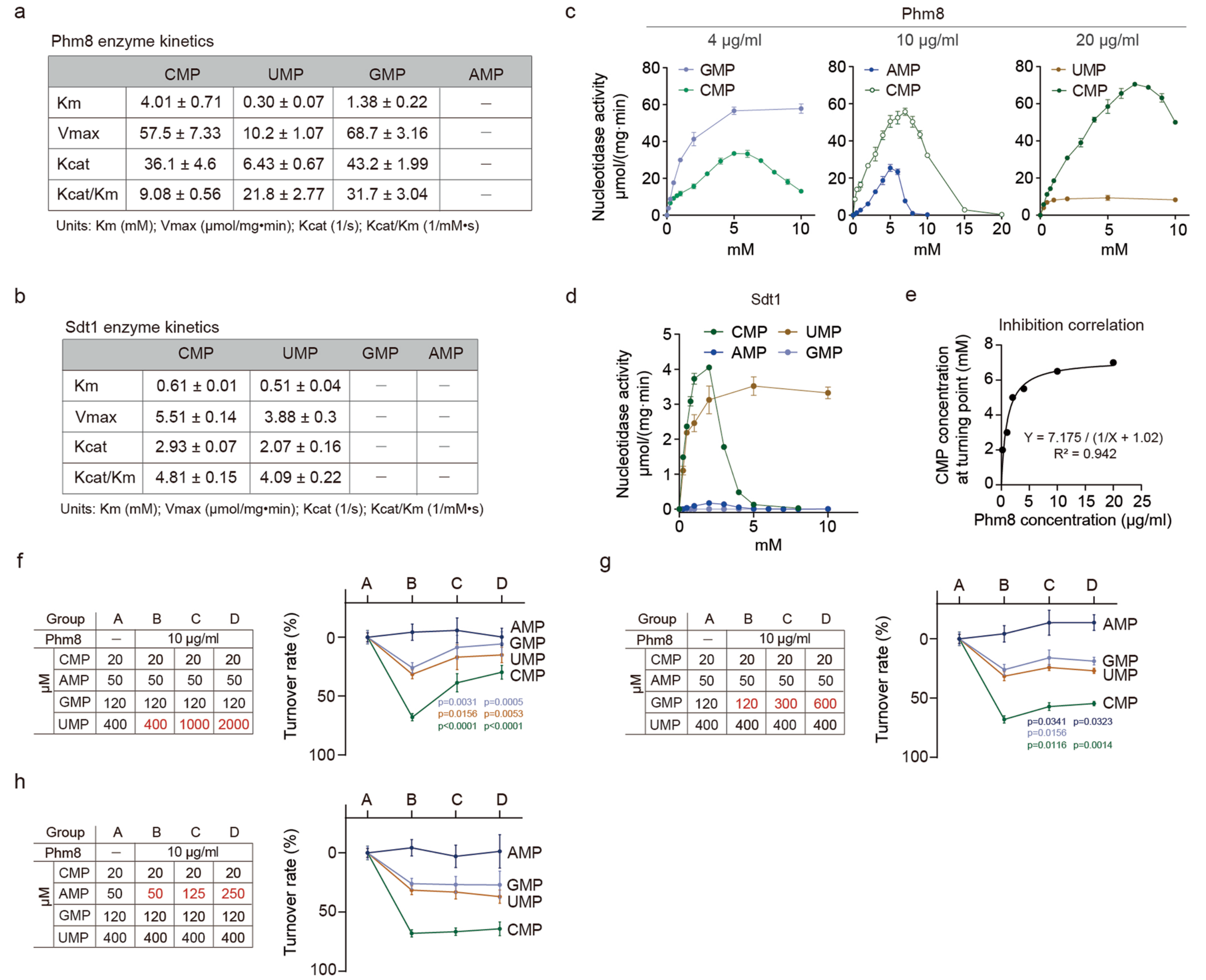

Phm8 enzyme kinetics

	CMP	UMP	GMP	AMP
Km	4.01 ± 0.71	0.30 ± 0.07	1.38 ± 0.22	—
Vmax	57.5 ± 7.33	10.2 ± 1.07	68.7 ± 3.16	—
Kcat	36.1 ± 4.6	6.43 ± 0.67	43.2 ± 1.99	—
Kcat/Km	9.08 ± 0.56	21.8 ± 2.77	31.7 ± 3.04	—

Units: Km (mM); Vmax (µmol/mg•min); Kcat (1/s); Kcat/Km (1/mM•s)

Sdt1 enzyme kinetics

	CMP	UMP	GMP	AMP
Km	0.61 ± 0.01	0.51 ± 0.04	—	—
Vmax	5.51 ± 0.14	3.88 ± 0.3	—	—
Kcat	2.93 ± 0.07	2.07 ± 0.16	—	—
Kcat/Km	4.81 ± 0.15	4.09 ± 0.22	—	—

Units: Km (mM); Vmax (µmol/mg•min); Kcat (1/s); Kcat/Km (1/mM•s)

f

Group		A	B	C	D
Phm8		—	10 µg/ml		
µM	CMP	20	20	20	20
	AMP	50	50	50	50
	GMP	120	120	120	120
	UMP	400	400	1000	2000

g

Group		A	B	C	D
Phm8		—	10 µg/ml		
µM	CMP	20	20	20	20
	AMP	50	50	50	50
	GMP	120	120	300	600
	UMP	400	400	400	400

h

Group		A	B	C	D
Phm8		—	10 µg/ml		
µM	CMP	20	20	20	20
	AMP	50	50	125	250
	GMP	120	120	120	120
	UMP	400	400	400	400

Extended Data Fig. 7 | CMP hydrolysis enzymes are subject to substrate inhibition. (**a**,**b**) Enzyme kinetics of Phm8 (**a**) and Sdt1 (**b**) against NMPs. Note that kinetic curves of Phm8 against AMP were shown in **c**. These curves did not fit with a standard Michaelis–Menten equation and thus did not generate numeric values for kinetic parameters. Sdt1 showed no activity against GMP and AMP. (**c**) Nucleotidase activity curves of purified Phm8 against CMP, GMP, AMP and UMP with indicated amounts of the enzyme. Data are represented as mean ± SD (n = 3; n = independent experiments). (**d**) Nucleotidase activity curves of purified Sdt1 against CMP, GMP, AMP and UMP. Sdt1 was used at 80 µg/ml for AMP and GMP, 40 µg/ml for CMP and 26.67 µg/ml for GMP. Data are represented as mean ± SD (n = 3; n = independent experiments). (**e**) Nonlinear regression fitting showing the relationship between the turning point of maximal nucleotidase activity and Phm8 concentration. (**f**–**h**) Turnover rates of CMP, AMP, GMP and UMP in a composite mixture of NMPs. Group A represents a negative control without Phm8; Group B–D represent mixture conditions containing 10 µg/ml Phm8, with increasing amounts of UMP (**f**), GMP (**g**) and AMP (**h**). Data are represented as mean ± SD (n = 4; n = independent experiments).

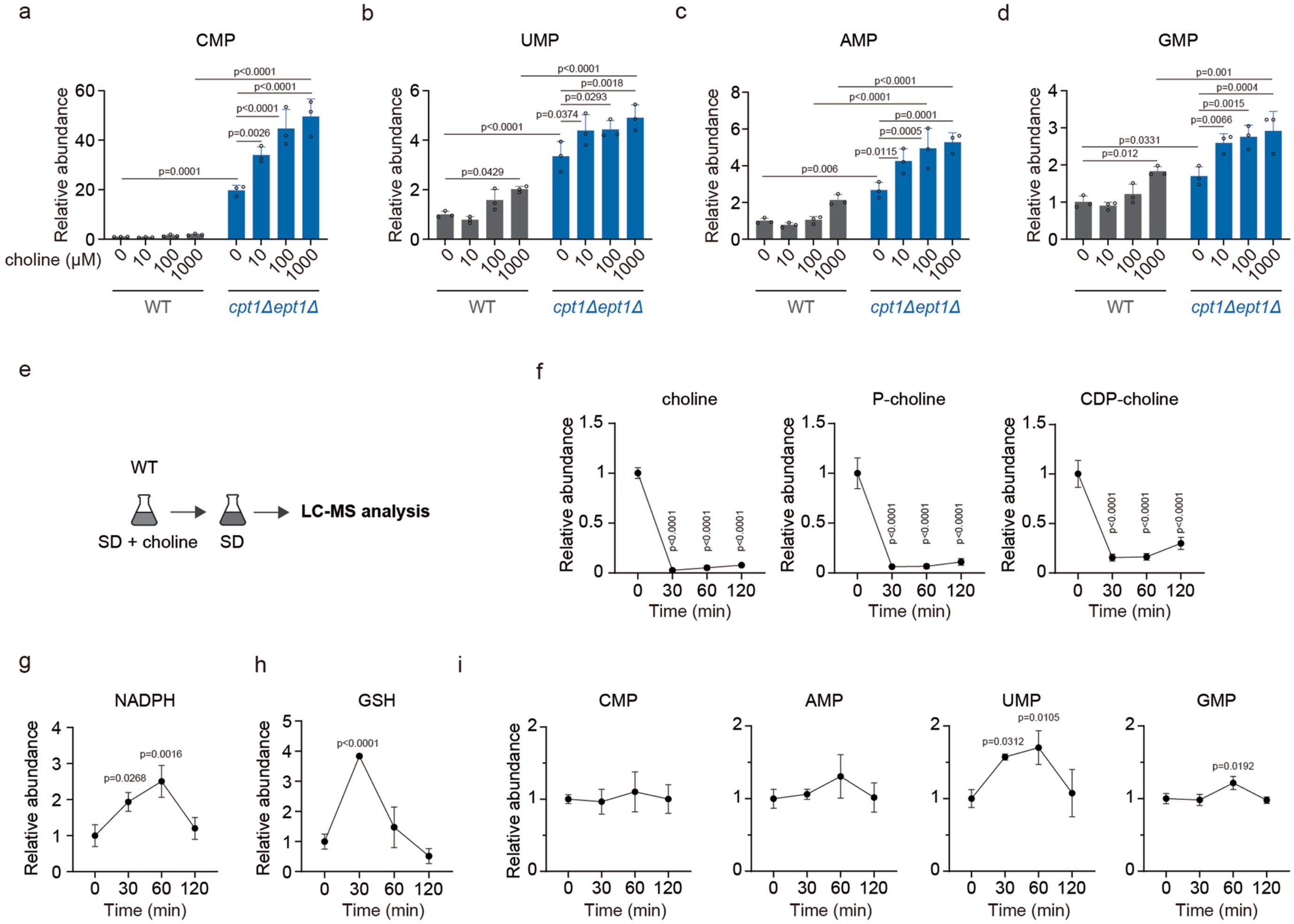

Extended Data Fig. 8 | Effects of exogenous choline on cellular nucleotide metabolism and reductive capacity. (**a**–**d**) Relative abundance of CMP (**a**), UMP (**b**), AMP (**c**) and GMP (**d**) in WT and *cpt1Δept1Δ* cells in minimal medium with different choline supplementation. Data are represented as mean ± SD (n = 3; n = biologically independent samples). (**e**) Experimental setup for switching cells from SD medium with 1 mM choline to SD minimal medium. (**f**) Relative abundance of choline, phosphocholine (P-choline) and CDP-choline in WT cells after switching to choline-free medium. Data are represented as mean ± SD (n = 3; n = biologically independent samples). (**g**,**h**) Relative abundance of NADPH (**g**) and GSH (**h**) levels during the removal of exogenous choline. Data are represented as mean ± SD (n = 3; n = biologically independent samples). (**i**) Relative abundance of CMP, AMP, UMP and GMP in WT cells after switching to choline-free medium. Data are represented as mean ± SD (n = 3; n = biologically independent samples).

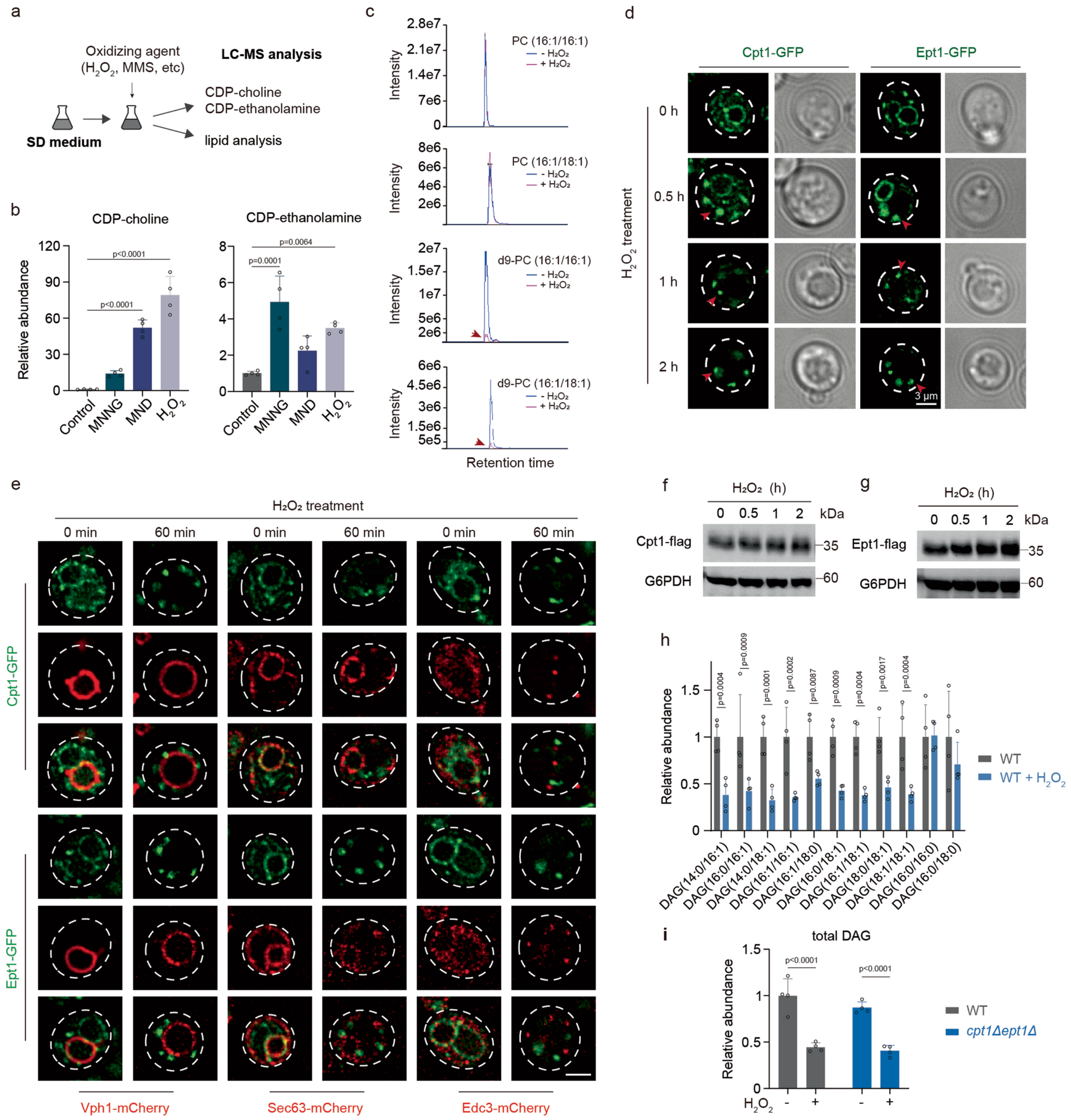

Extended Data Fig. 9 | Oxidative stress inhibits AAPT step in the Kennedy pathway. (**a**) Schematic depicting metabolite and lipid analyses of cells exposed to oxidizing agents. (**b**) Relative abundance of CDP-choline and CDP-ethanolamine in WT cells exposed to N-methyl-N'-nitro-N-nitrosoguanidine (MNNG; 5 mM), menadione (MND; 1 mM) and H_2O_2 (5 mM) for 1 h. Data are presented as mean ± SD (n = 4; n = biologically independent samples). (**c**) The ion chromatogram of PC and d9-labeled PC species before and after H_2O_2 treatment. (**d**) Live cell imaging of Cpt1-GFP and Ept1-GFP under H_2O_2 treatment. (**e**) Live cell imaging of Cpt1-GFP and Ept1-GFP under H_2O_2 treatment. Vph1-mCherry is a vacuole marker, Sec63-mCherry is an ER marker and Edc3-mCherry is a P-body marker. Scale bar = 3 µm. (**f**,**g**) Western blots assaying protein levels of Cpt1-flag (**f**) and Ept1-flag (**g**) under H_2O_2 treatment. (**h**) Relative levels of DAG species in WT cells with or without a 60-min treatment of H_2O_2. Data are presented as mean ± SD (n = 4; n = biologically independent samples). (**i**) The total amount of DAG in cells with or without a 60-min treatment of H_2O_2. Data are presented as mean ± SD (n = 4; n = biologically independent samples).

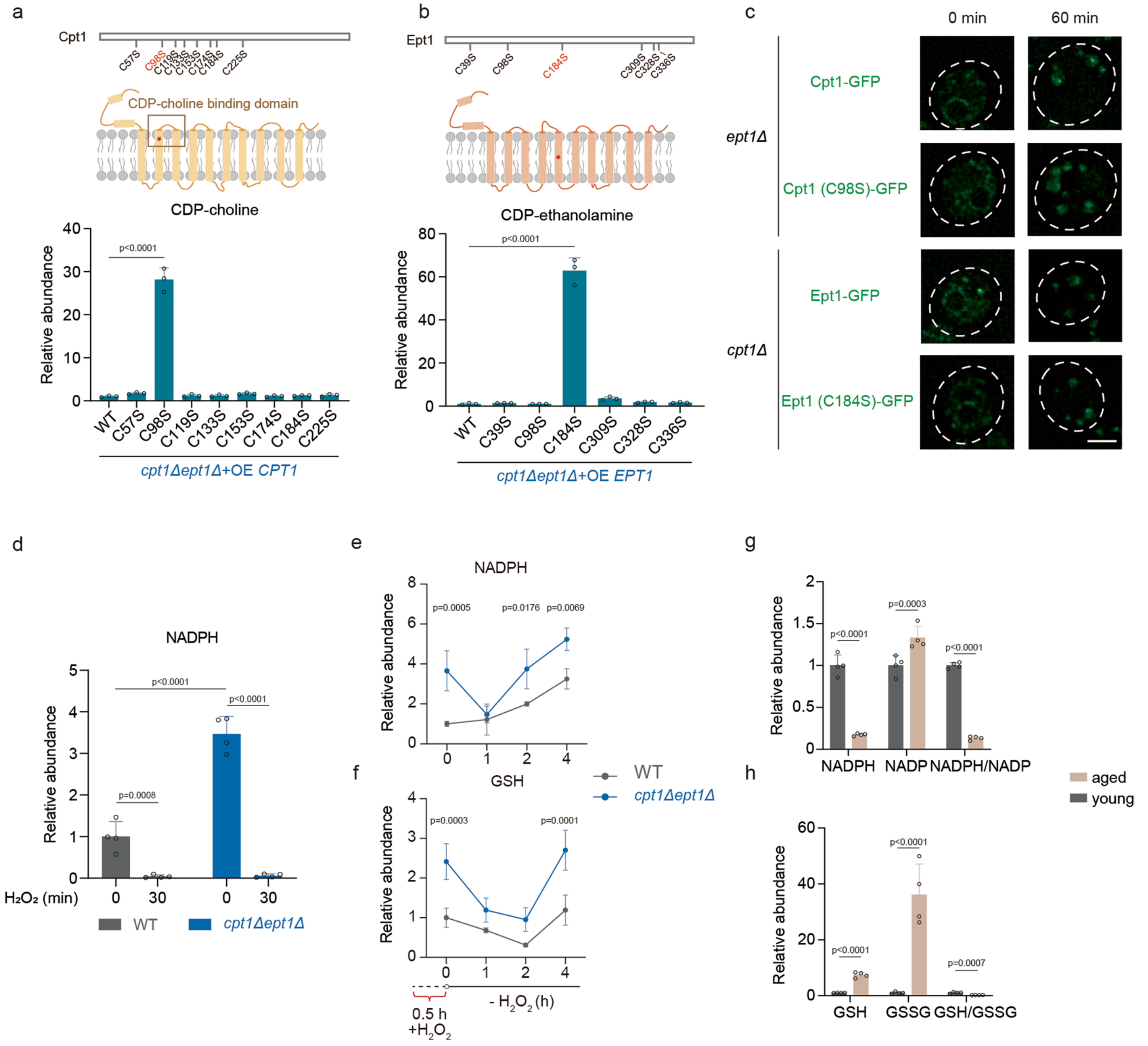

Extended Data Fig. 10 | Defective Kennedy pathway demonstrates enhanced capacities in restoring cellular reductive capacity after oxidative stress. (**a**) The position of C98 residue in Cpt1 and relative abundance of CDP-choline in all Cpt1 cysteine residue mutants in *cpt1Δept1Δ* cells. (**b**) The position of C184 residue in Ept1 and relative abundance of CDP-ethanolamine in all Ept1 cysteine residue mutants in *cpt1Δept1Δ* cells. (**c**) Live cell imaging of Cpt1-GFP and Cpt1 (C98S)-GFP in *ept1Δ* cells and Ept1-GFP and Ept1 (C184S)-GFP in *cpt1Δ* cells before and after H_2O_2 treatment. Scale bar = 3 µm. (**d**) Relative abundance of NADPH in WT and *cpt1Δept1Δ* cells before and after H_2O_2 treatment. Data are represented as mean ± SD (n = 4; n = biologically independent samples). (**e**,**f**) Levels of NADPH (**e**) and GSH (**f**) in WT and *cpt1Δept1Δ* cells switched to fresh minimal medium for indicated times after a 30-min H_2O_2 treatment. (**g**) Relative abundance of NADPH, $NADP^+$ and NADPH/$NADP^+$ ratio in aged and young WT cells. Data are presented as mean ± SD (n = 4; n = biologically independent samples). (**h**) Relative abundance of GSH, GSSG and GSH/GSSG ratio in aged and young WT cells. Data are presented as mean ± SD (n = 4; n = biologically independent samples).

nature portfolio

Corresponding author(s): Cunqi Ye

Last updated by author(s): May 8, 2024

Reporting Summary

Nature Portfolio wishes to improve the reproducibility of the work that we publish. This form provides structure for consistency and transparency in reporting. For further information on Nature Portfolio policies, see our Editorial Policies and the Editorial Policy Checklist.

Statistics

For all statistical analyses, confirm that the following items are present in the figure legend, table legend, main text, or Methods section.

n/a	Confirmed	
☐	☒	The exact sample size (*n*) for each experimental group/condition, given as a discrete number and unit of measurement
☐	☒	A statement on whether measurements were taken from distinct samples or whether the same sample was measured repeatedly
☐	☒	The statistical test(s) used AND whether they are one- or two-sided *Only common tests should be described solely by name; describe more complex techniques in the Methods section.*
☒	☐	A description of all covariates tested
☒	☐	A description of any assumptions or corrections, such as tests of normality and adjustment for multiple comparisons
☐	☒	A full description of the statistical parameters including central tendency (e.g. means) or other basic estimates (e.g. regression coefficient) AND variation (e.g. standard deviation) or associated estimates of uncertainty (e.g. confidence intervals)
☐	☒	For null hypothesis testing, the test statistic (e.g. *F*, *t*, *r*) with confidence intervals, effect sizes, degrees of freedom and *P* value noted *Give P values as exact values whenever suitable.*
☒	☐	For Bayesian analysis, information on the choice of priors and Markov chain Monte Carlo settings
☒	☐	For hierarchical and complex designs, identification of the appropriate level for tests and full reporting of outcomes
☒	☐	Estimates of effect sizes (e.g. Cohen's *d*, Pearson's *r*), indicating how they were calculated

Our web collection on statistics for biologists contains articles on many of the points above.

Software and code

Policy information about availability of computer code

Data collection	Intracellular metabolites were measured using the QTRAP 6500+ System, ABSCIEX. The raw data were extracted with the software Analyst v1.7.2 and OS v2.0 from SCIEX; Real-time PCR was performed in a Bio-Rad CFX96 Connect device.
Data analysis	The normalized abundances of metabolites were log-transformed, centered about the median, and clustered by Spearman rank correlation algorithm using Cluster 3, and heat maps were obtained by the software Treeview 1.2.0.

For manuscripts utilizing custom algorithms or software that are central to the research but not yet described in published literature, software must be made available to editors and reviewers. We strongly encourage code deposition in a community repository (e.g. GitHub). See the Nature Portfolio guidelines for submitting code & software for further information.

Data

Policy information about availability of data

All manuscripts must include a data availability statement. This statement should provide the following information, where applicable:

- Accession codes, unique identifiers, or web links for publicly available datasets
- A description of any restrictions on data availability
- For clinical datasets or third party data, please ensure that the statement adheres to our policy

All data supporting the findings of this study presented in this article are available within the article, supplementary information and source data. In addition, the

RNA-seq data reported in this publication have been deposited in NCBI's Gene Expression Omnibus (GEO) and are accessible through GEO Series accession number GSE269275 and GSE269277. Source data are provided with this paper.

Research involving human participants, their data, or biological material

Policy information about studies with human participants or human data. See also policy information about sex, gender (identity/presentation), and sexual orientation and race, ethnicity and racism.

Reporting on sex and gender	N/A
Reporting on race, ethnicity, or other socially relevant groupings	N/A
Population characteristics	N/A
Recruitment	N/A
Ethics oversight	N/A

Note that full information on the approval of the study protocol must also be provided in the manuscript.

Field-specific reporting

Please select the one below that is the best fit for your research. If you are not sure, read the appropriate sections before making your selection.

☒ Life sciences ☐ Behavioural & social sciences ☐ Ecological, evolutionary & environmental sciences

For a reference copy of the document with all sections, see nature.com/documents/nr-reporting-summary-flat.pdf

Life sciences study design

All studies must disclose on these points even when the disclosure is negative.

Sample size	Sample size was chosen based on experimental variability and the requirement of experimental samples for statistical analysis. At least three biological replicates per group were collected to perform statistical testing, which is sufficient for a minimal data set underlying the figures provided in the paper in order to support and interpret our central findings. Detailed n is indicated in the figure legends. No statistical method was used to determine the sample size.
Data exclusions	No data or samples were excluded from the analysis.
Replication	Experiments were performed at least twice to make sure that the results are reproducible, and representative data are shown. All attempts at replication were successful. Details are shown in Method.
Randomization	All samples were randomly allocated to experimental groups and processed.
Blinding	For the analyses of the qPCR data and cellular metabolites, blinding was not necessary since these analyses were observer independent. Blinding was performed during the acqusition of the metabolic raw data. The researcher who inspected the spectra intensities were blinded to the sample information. Western blotting was not performed blind to load samples by order.

Reporting for specific materials, systems and methods

We require information from authors about some types of materials, experimental systems and methods used in many studies. Here, indicate whether each material, system or method listed is relevant to your study. If you are not sure if a list item applies to your research, read the appropriate section before selecting a response.

Materials & experimental systems

n/a	Involved in the study	
☐	☒	Antibodies
☐	☒	Eukaryotic cell lines
☒	☐	Palaeontology and archaeology
☒	☐	Animals and other organisms
☒	☐	Clinical data
☒	☐	Dual use research of concern
☒	☐	Plants

Methods

n/a	Involved in the study	
☒	☐	ChIP-seq
☒	☐	Flow cytometry
☒	☐	MRI-based neuroimaging

Antibodies

Antibodies used	mouse anti-FLAG M2 antibody (Sigma, Cat# F3165, dilution, 1:5000) and rabbit anti-G6PDH (Sigma, Cat#A9521, dilution, 1:5000),.
Validation	All antibodies are commercially available and were validated as follows: https://www.sigmaaldrich.cn/CN/zh/product/sigma/f3165 https://www.sigmaaldrich.cn/CN/zh/product/sigma/a9521

Eukaryotic cell lines

Policy information about cell lines and Sex and Gender in Research

Cell line source(s)	The prototrophic CEN.PK strain of the budding yeast S. cerevisiae background was used in all experiments.
Authentication	None of the cell lines used were authenticated.
Mycoplasma contamination	The yeast cells were not tested for mycoplasma.
Commonly misidentified lines (See ICLAC register)	No commonly misidentified cell lines were involved in this study.

Plants

Seed stocks	N/A
Novel plant genotypes	N/A
Authentication	N/A